REPORT DOCUMENTATION PAGE

Form Approved OMB NO. 0704-0188

The public reporting burden for this collection of information is estimated to average 1 hour per response, including the time for reviewing instructions, searching existing data sources, gathering and maintaining the data needed, and completing and reviewing the collection of information. Send comments regarding this burden estimate or any other aspect of this collection of information, including suggesstions for reducing this burden, to Washington Headquarters Services, Directorate for Information Operations and Reports, 1215 Jefferson Davis Highway, Suite 1204, Arlington VA, 22202-4302. Respondents should be aware that notwithstanding any other provision of law, no person shall be subject to any oenalty for failing to comply with a collection of information if it does not display a currently valid OMB control number.
PLEASE DO NOT RETURN YOUR FORM TO THE ABOVE ADDRESS.

1. REPORT DATE (DD-MM-YYYY)	2. REPORT TYPE	3. DATES COVERED (From - To)
04-01-2016	MS Thesis	-

4. TITLE AND SUBTITLE

On the formation of Friedlander waves in a compressed-gas driven shock tube

5a. CONTRACT NUMBER

5b. GRANT NUMBER

W911NF-13-D-0001

5c. PROGRAM ELEMENT NUMBER

611104

6. AUTHORS

A. Tasissa, M. Hautefeuille, J. Fitek, R. Radovitzky

5d. PROJECT NUMBER

5e. TASK NUMBER

5f. WORK UNIT NUMBER

7. PERFORMING ORGANIZATION NAMES AND ADDRESSES

Massachusetts Institute of Technology (MIT
77 Massachusetts Ave.
NE18-901
Cambridge, MA 02139 -4307

8. PERFORMING ORGANIZATION REPORT NUMBER

9. SPONSORING/MONITORING AGENCY NAME(S) AND ADDRESS (ES)

U.S. Army Research Office
P.O. Box 12211
Research Triangle Park, NC 27709-2211

10. SPONSOR/MONITOR'S ACRONYM(S)
ARO

11. SPONSOR/MONITOR'S REPORT NUMBER(S)

63760-CH-ISN.382

12. DISTRIBUTION AVAILIBILITY STATEMENT

Approved for public release; distribution is unlimited.

13. SUPPLEMENTARY NOTES

The views, opinions and/or findings contained in this report are those of the author(s) and should not contrued as an official Department of the Army position, policy or decision, unless so designated by other documentation.

14. ABSTRACT

Abstract unavailable

15. SUBJECT TERMS

shock tube, Friedlander waves

16. SECURITY CLASSIFICATION OF:			17. LIMITATION OF ABSTRACT	15. NUMBER OF PAGES	19a. NAME OF RESPONSIBLE PERSON
a. REPORT	b. ABSTRACT	c. THIS PAGE			John Joannopoulos
UU	UU	UU	UU		19b. TELEPHONE NUMBER 617-253-4806

Report Title

On the formation of Friedlander waves in a compressed-gas driven shock tube

ABSTRACT

Abstract unavailable

On the formation of Friedlander waves in a compressed gas driven shock tube

by

Abiy Tasissa

B.S., Mathematics(2012)
Massachusetts Institute of Technology

Submitted to the Department of Aeronautics and Astronautics
in partial fulfillment of the requirements for the degree of

Master of Science in Aeronautics and Astronautics

at the

MASSACHUSETTS INSTITUTE OF TECHNOLOGY

June 2014

ARCHIVES
MASSACHUSETTS INSTITUTE OF TECHNOLOGY
JUN 16 2014
LIBRARIES

© Massachusetts Institute of Technology 2014. All rights reserved.

Signature redacted

Author .....
Department of Aeronautics and Astronautics
May 22, 2014

Signature redacted

Certified by .....
Raúl Radovitzky
Professor of Aeronautics and Astronautics
Thesis Supervisor

Signature redacted

Accepted by .....
Paulo C. Lozano
Associate Professor of Aeronautics and Astronautics
Chair, Graduate Program Committee

On the formation of Friedlander waves in a compressed gas driven shock tube

by

Abiy Tasissa

Submitted to the Department of Aeronautics and Astronautics
on May 22, 2014, in partial fulfillment of the
requirements for the degree of
Master of Science in Aeronautics and Astronautics

Abstract

Compressed gas driven shock tubes have become popular as a laboratory-scale replacement for field blast tests. The well-known initial structure of the Riemann problem eventually evolves into a shock structure resembling a Friedlander wave. In this thesis, we develop an analytical model to predict its key characteristics: location where the wave first forms, peak over-pressure, decay time and impulse. The approach is based on combining the solutions of the two different types of wave interactions that arise in the shock tube after the family of rarefaction waves in the Riemann solution interacts with the closed end of the tube. The results of the analytical model are verified against numerical simulations obtained with a finite volume method. The model furnishes a rational approach to relate shock tube parameters to desired blast wave characteristics, and thus constitutes a useful tool for the design of shock tubes for blast testing.

Thesis Supervisor: Raúl Radovitzky
Title: Professor of Aeronautics and Astronautics

Acknowledgments

I would like to thank my research advisor Prof. Raúl Radovitzky for his support in the last two years. I am grateful for the opportunity he gave me to explore possible topics before settling on the topic of my thesis. Thanks to his guidance, I have also learned a lot about writing papers and presenting. For all these and beyond, I am grateful.

This thesis wouldn't have taken its current form without the help of Dr. Martin Hautefeuille. From our long discussions on the thesis problem to writing clean codes and technical papers, Dr. Martin was always willing to help. I have learned a lot under his mentorship and I am thankful for all the time he invested in me.

I should express my appreciation to the group members Andrew Seagraves, Aurelie Jean, Gauthier Becker, Lei Qiao, Michael Tupek, Michelle Nyein and Wendy Pino.

I would like to thank Adrian Rosolen for taking an interest in my studies and giving me support whenever I needed it. I would miss our late night schedules and chats over coffee. I would also like to thank Brandon Talamini who was always very willing to help and has a lot of insights on many topics. I know that and I wish you will become a great researcher.

I would like to thank Professor Jared Speck, Professor Gabrielle Stoy and Professor Michael Driscoll for their kind help through the years. I appreciate you took an interest in my personal development and future.

I would like to thank my MIT friends Alban Cobi, Asmamaw Wassie, Austin Anderson and Edward Flores. You all have been quite instrumental to my happiness and success. I am grateful to Adnan Zolj for being so kind and caring to me for all these years. I am thankful to my friend Mukul for always making yourself available anytime. I will miss our coffee time. My deep gratitude to my friend Wegene for bringing home closer to me. Thanks to Nasruddin Nazerali, Deriba Olana, Gash Solomon and Gash Salah for inviting me over to "Norfolk College" and making me feel at home.

I am thankful to my home town "Merkato" where I learned the love of life, hard work and most importantly self respect.

To my family whom I haven't seen for six years, thank you supporting me during all these years. This would have been impossible without your love. I would like to thank my sister Meron Tasissa who has been very caring to me here in Boston. I would like to thank my mother Askale Etana for all her prayers. Above all, I would like to thank my long time friend and my father Fekadu Tasissa. Without you "Gashe", all this wouldn't have been possible. I am forever grateful for all the sacrifices. I hope you are happy of who I have become.

To my love Roza Tesfaye: words cannot express how much you mean to me and I am grateful that you have been there for me all along.

I have come very far from what I once imagined. For all the journey, I owe it all to God.

THIS PAGE INTENTIONALLY LEFT BLANK

Contents

List of Figures

THIS PAGE INTENTIONALLY LEFT BLANK

List of Tables

THIS PAGE INTENTIONALLY LEFT BLANK

Chapter 1

Introduction

In addition to their many uses in the science and engineering of compressible flows, shock tubes have recently become popular as devices to generate shock waves whose structure resembles a real blast wave such as produced by the detonation of explosive charges, e.g. [1, 2, 3, 4, 5, 6, 7, 8, 9, 10]. Lab-scale tests using shock tubes are convenient surrogates for field blast tests as they provide better precision and variable control, increased safety, and re The basic functioning of a shock tube in its traditional configuration is well understood, e.g. [11]: pressurized gas in a driver section is suddenly released by the rupture of a membrane, leading to a well known shock structure comprised of a shock wave, a contact discontinuity, and a family of rarefaction waves [12]. What is observed experimentally is that, for sufficiently long shock tubes, this wave structure eventually evolves into a shape resembling an air blast wave. What has received less attention is the process by which this happens and the relation between shock tube parameters and the characteristics of the resulting "blast wave".

In fact, it has been well established that, despite their popularity as blast test surrogates, shock tubes sometimes fail to generate true blast waves [6]. Instead, if the shock tube parameters are not designed "correctly", the shock waves obtained have a tendency to adopt trapezoidal shapes where the peak pressure plateaus before it decays as blast waves do, [1] .

Knowing the location where the blast wave initially forms is important for properly

placing the target in animal studies of blast-induced Traumatic Brain Injury, [5]. However, estimates of the location of the onset of the blast wave are mostly empirical. In [8, 4], Bass and coworkers resort to the rule of thumb that a blast wave forms at distance equal to 10 times the diameter of the tube. Courtney et al [6], state that the driven section of the tube should be much longer (60 times the diameter of the tube). It is therefore clear that there is a need for developing a rational approach for designing shock tubes for lab-scale blast testing.

Previous efforts to analyze the formation of Friedlander waves in shock tubes have been based on Computational Fluid Dynamics (CFD). CFD simulations have shown the evolution from the Riemann shock wave structure to the eventual formation of a shock wave akin to a Friedlander blast wave. The accuracy of CFD numerical tools has been validated by comparing the time evolution of the pressure at specific location in the tube with experimental pressure sensor data, [4]. CFD has also been instrumental in describing the flow conditions as the wave approaches and goes past the open end of the tube, [13, 7].

In this thesis, we develop an analytical model that provides a functional relationship between shock tube parameters (driver section length, pressure and driver gas) and the sought blast wave characteristics in closed mathematical form. As in many other areas of engineering and science, an analytical description, if available, is highly desirable in the design and configuration of the testing device, as it eliminates the need for costly parametric studies using numerical solution methods. Moreover, analytical models enable the immediate solution of the design (inverse) problem, i.e. how to configure the problem inputs to obtain a desired set of outcomes. In the specific case of lab-scale blast testing, this translates to: what is the required set of shock tube configuration parameters (initial pressure, driver section length and gas type) to produce a surrogate blast wave with given characteristics (free-field overpressure and decay time, or alternatively explosive energy and offset), and what is the minimum required tube length?

The analytical model is derived by analyzing two types of nonlinear wave interactions that arise as the family of rarefaction waves in the initial Riemann problem

reflects from the closed end of the tube to eventually catch up with the shock wave. The first problem is concerned with the reflection of the family of centered rarefaction waves (rarefaction fan) off the closed end of the driver section. The solution of the flow in this so-called buffer region, [14], is known to be non-simple and has been derived using Riemann invariants, leading to a second-order hyperbolic partial differential equation (PDE) of the Euler-Poisson type, [12]. For arbitrary gas specific heat ratios, the solution to this PDE can be expressed as a hypergeometric function which gives the position of the interacting waves as a function of time in implicit form. We propose an alternative derivation resulting in an Euler-Darboux PDE whose solution in the important cases of air and helium can be written in terms of much simpler rational functions. This, in turn, is convenient for the next steps in the analysis. The simplified solution is used to find the exit time and position where the reflected head wave intersects the incident tail wave, at which point the head and subsequent reflected waves enter a simple region (straight characteristic lines) with known propagation speed.

The second problem involves the interaction of these reflected waves when they reach the contact discontinuity moving in the direction of the shock. The flow in this second buffer region can be analyzed using Courant's solution for a simple wave interacting with a contact discontinuity [15]. A discrete consideration of equally-spaced incident waves combined with a linearized analysis of their propagation velocity furnishes a discrete estimate of the curved geometry of the modified contact interface, as well as the time, position and propagation speed of the simple waves transmitted across it. Finally, this information is used to determine the location and time when the head wave encounters the shock front, which is considered the onset of the blast wave structure. The subsequent evolution of the flow at that location (pressure decay) is estimated by considering the arrival time and pressure of a discrete set of trailing waves. The final result of the analysis is explicit formulas relating shock tube parameters (driver's section length and compressed gas state) to blast wave characteristics (peak overpressure, decay time and impulse). In particular, the model furnishes the very important required driver section length as a function of aforementioned shock

tube parameters and also shows its independence of the shock tube diameter contrary to what was previously believed [8, 6].

The structure of the thesis is as follows: Chapter 2 will present the fundamentals. In chapters 3 and 4, we discuss the analysis of the different wave interactions and develop analytical estimates of the characteristics of the pressure profile at the onset of the Friedlander wave. We present numerical and analytical results in chapter 5 and conclude in chapter 6.

Chapter 2

Fundamentals

In this chapter, we provide necessary background information for the subsequent analysis specifically highlighting key ideas from thermodynamics and gas dynamics. We also present a very brief summary of the classic Riemann problem and show a derivation of the Riemann invariants. For results without derivations, the full details of what is presented here can be found in the classic books of Fermi [16], Landau and [17],Anderson[14] and Zeldovich[18].

2.1 Thermodynamics and Gas Dynamics

- *Ideal Gas*

  The thermodynamic quantities of interest in gas dynamics are pressure p, temperature T and volume V. These quantities are not independent and their relationship is given by the form:

  $$f(V, p, T) = 0$$

  The above relationship is what is known as the *equation of state*. The form of the function f depends on the choice of the gas. For ideal gases, the equation of state can be written as:

  $$pV = MRT \tag{2.1}$$

where M is the mass of the gas and R is the universal gas constant. We can also write this in an alternative form by dividing both sides by the mass of the gas:

$$pv = RT \tag{2.2}$$

where v is the specific volume of the gas ($v = \frac{1}{\rho}$, ρ being the density of the gas).

- *Internal Energy and Enthalpy*

  On a microscopic scale, gas is a collection of molecules in random motion. There is kinetic energy from the movement of the molecules and potential energy from the intermolecular forces. The internal energy, E, is the sum of the kinetic and potential energies. The enthalpy, h, defined per unit mass, is $h = e + pv$ where e is the internal energy per unit mass. For a general gas, we have

$$e = e(T, v)$$
$$h = h(T, p)$$
$$de = c_v dT$$
$$dh = c_p dT$$

  where c_v is the specific heat at constant volume and c_p is the specific heat at constant pressure. Note that c_v and c_p are functions of temperature.

- *Thermally Perfect Gas*

  If the gas molecules are not chemically reacting and the intermolecular forces are ignored, the gas is thermally perfect. This implies that the internal energy and enthalpy are functions of temperature only.

$$e = e(T)$$
$$h = h(T)$$
$$de = c_v dT$$
$$dh = c_p dT$$

- *Calorically Perfect Gas*

  A calorically perfect gas is a thermally perfect gas with constant specific heats. The enthalpy and the internal energy respectively are given by

$$\begin{aligned} e &= c_v T \\ h &= c_p T \end{aligned} \tag{2.3}$$

- *Heat Capacity Ratio*

  The heat capacity ratio is defined as:

$$\gamma = \frac{c_p}{c_v} \tag{2.4}$$

  We note here the value of γ for the two most common driver gases for shock tubes. For air $\gamma = 1.4$ and for helium $\gamma = \frac{5}{3}$.

- *Isentropic Relations*

  Consider a thermodynamic process proceeding from some initial state to a final state. The following relations hold true for an isentropic(constant entropy) process.

$$\frac{p_2}{p_1} = \left(\frac{\rho_2}{\rho_1}\right)^{\gamma} = \left(\frac{T_2}{T_1}\right)^{\frac{\gamma}{\gamma-1}} \tag{2.5}$$

  The subscripts 1 and 2 refer to the initial and final states respectively.

- *Material Derivative*

  Consider a fluid particle as it moves through a flow field. The time rate of change of a fluid property at a fixed position in space is given by $\frac{\partial}{\partial t}$. On the other hand, the time rate of change of a fluid property with respect to the moving fluid particle is described by the substantial derivative $\frac{D\rho}{Dt}$. The two can be related as follows:

$$\frac{D}{Dt} = \frac{\partial}{\partial t} + u \cdot \nabla \tag{2.6}$$

  where u is the velocity of the particle.

- *Adiabatic Process*

  A thermodynamic process no external heat source is added or removed is adiabatic. The adiabatic flow condition is the statement that the material derivative of the specific entropy remains constant.

$$\frac{DS}{Dt} = 0 \tag{2.7}$$

  where S is the specific entropy.

- Specification of a state variable

  In Thermodynamics, a unique specification of a state variable requires exactly two other state variables. For instance, the density of a gas can be determined given the entropy and pressure.

$$\rho = \rho(p, s) \tag{2.8}$$

- *Speed of Sound*

  The sound speed a is the speed at which small or infinitesimal perturbations are propagated through a gas. It is given by

$$a = \sqrt{\left(\frac{\partial p}{\partial \rho}\right)_s} \tag{2.9}$$

  The subscript s denotes that the sound wave process is isentropic. For a calorically perfect gas, (2.9) reduces to:

$$a = \sqrt{\gamma RT} \tag{2.10}$$

  Using (2.2), (2.10) reduces to:

$$a = \sqrt{\frac{\gamma p}{\rho}} \tag{2.11}$$

- *Mach Number*

The Mach number is the ratio of the flow speed to the speed of the sound.

$$M = \frac{u}{a}$$

If $M > 1$, the flow is supersonic and if $M < 1$ the flow is subsonic.

- *Conservation Equations*

  In gas dynamics, the conservation of mass, momentum and energy can be described by the following equations:

$$\frac{D\rho}{Dt} + \rho\nabla \cdot u = 0 \qquad \text{Continuity} \tag{2.12}$$

$$\rho\frac{Du}{Dt} = -\nabla p \qquad \text{Motion} \tag{2.13}$$

$$\frac{De}{Dt} + p\frac{Dv}{Dt} = Q \qquad \text{Energy} \tag{2.14}$$

  Here Q is the energy generated per unit mass per unit time and e is the specific internal energy.

2.2 Riemann problem

The Riemann problem is an initial value problem given by

$$u_t + f(u)_x = 0$$
$$u(x, 0) = u_0(x)$$

Here u refers to a quantity of interest(density, concentration,...) and $f(u)$ is the flux function. The initial condition $u(x, 0)$ is two constant states u_L and u_R separated by a jump discontinuity at $x = 0$ i.e

$$u_0(x) = u_L \text{ if } x \leq 0$$
$$u_0(x) = u_R \text{ if } x \geq 0$$

The the initial value problem as posed above admits a unique solution[19]. Given the above setup, the Riemann problem is equivalent to the determination of $u(x,t)$ for $t > 0$. In other words, we want to determine u after the discontinuity is removed at all times. In the context of gas dynamics, the Riemann problem reduces to the shock tube problem.

A shock tube has two sections separated by a diaphragm. The region to the left of the diaphragm, initially at a constant high pressure, is called the *driver section.* The region to the right of the diaphragm, initially at a constant low pressure, is called the *driven section.* At $t = 0$, the driver and driven sections correspond to the initial conditions for the Riemann problem. The diaphragm is analogous to the jump discontinuity. Hence the problem becomes that of determining the flow in the shock tube once the diaphragm is broken. The solution for the flow, originally due to Riemann, is a right propagating shock wave separated from a left going family of rarefaction waves by a contact interface. [14].

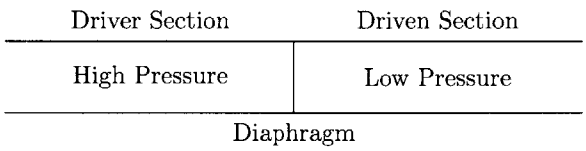

Figure 2-1: Schematic of a Shock Tube.

2.3 Derivation of the Riemann invariants

The starting point is consideration of the continuity equation (2.12) and equation of motion (2.13) for an inviscid flow. In the case of one dimensional flow, the equations reduce to:

$$\frac{D\rho}{Dt} + \rho\frac{\partial u}{\partial x} = 0 \tag{2.15}$$

$$p\frac{Du}{Dt} = -\frac{\partial p}{\partial x} \tag{2.16}$$

Using (2.8) and by considering the substantial derivative $\frac{D\rho}{Dt}$, the multivariable chain rule is applied to obtain:

$$\frac{D\rho}{Dt} = \left(\frac{Dp}{Dt}\right)\left(\frac{\partial\rho}{\partial p}\right)_s + \left(\frac{Ds}{Dt}\right)\left(\frac{\partial\rho}{\partial s}\right)_p \tag{2.17}$$

Using (2.7), (2.17) reduces to:

$$\frac{D\rho}{Dt} = \left(\frac{Dp}{Dt}\right)\left(\frac{\partial\rho}{\partial p}\right)_s \tag{2.18}$$

Using (2.9), substantial derivative of the density is:

$$\frac{D\rho}{Dt} = \frac{1}{c^2}\left(\frac{Dp}{Dt}\right) \tag{2.19}$$

Substituting (2.19) in the one dimensional continuity equation (2.15) and simplifying leads us to the following equation:

$$\frac{1}{\rho c}\frac{\partial p}{\partial t} + \frac{u}{\rho c}\frac{\partial p}{\partial x} + c\frac{\partial u}{\partial x} = 0 \tag{2.20}$$

Expanding the substantial derivative (2.6), the equation of motion (2.16) can be rewritten as follows:

$$\frac{\partial u}{\partial t} + u\frac{\partial u}{\partial x} + \frac{1}{\rho}\frac{\partial p}{\partial x} = 0 \tag{2.21}$$

Adding (2.20) to (2.21) gives::

$$\left((u+c)\frac{\partial u}{\partial x} + \frac{\partial u}{\partial t}\right) + \frac{1}{\rho c}\left(\frac{\partial p}{\partial t} + (u+c)\frac{\partial p}{\partial x}\right) = 0 \tag{2.22}$$

The characteristics are given by $\frac{dx}{dt} = (u+c)$ and denoted c_+ since their path is to the right. Subtracting (2.20) from (2.21) gives:

$$\left((u-c)\frac{\partial u}{\partial x} + \frac{\partial u}{\partial t}\right) - \frac{1}{\rho c}\left(\frac{\partial p}{\partial t} + (u-c)\frac{\partial p}{\partial x}\right) = 0 \tag{2.23}$$

The characteristics are given by $\frac{dx}{dt} = (u - c)$ and denoted c_- since their path is to the left. Along the c_+ characteristics, (2.22) reduces to

$$du + \frac{dp}{\rho c} = 0 \tag{2.24}$$

Along the c_- characteristics, (2.23) reduces to

$$du - \frac{dp}{\rho c} = 0 \tag{2.25}$$

Applying the isentropic relations (2.5) for a calorically perfect gas, the pressure density relationship is obtained:

$$p = k\rho^{\gamma} \text{ where } k \text{ is a constant}$$

Using (2.9):

$$\frac{dp}{d\rho} = k\gamma\rho^{\gamma-1} = c^2$$

It follows that

$$c = (k\gamma)^{\frac{1}{2}}\rho^{\frac{\gamma-1}{2}} \tag{2.26}$$

Integrating (2.24) along the c_+ characteristics

$$u + \int \frac{[k\gamma\rho^{\gamma-1}]d\rho}{\rho[(k\gamma)^{\frac{1}{2}}\rho^{\frac{\gamma-1}{2}}]} = r \quad \text{where } r \text{ is a constant}$$

Simplifying and applying (2.26)

$$u + \frac{2}{\gamma - 1}c = r$$

Using the same approach as above and integrating (2.25) along the c_- characteristics, the following equation will be obtained.

$$u - \frac{2}{\gamma - 1}c = s \quad \text{where } s \text{ is a constant}$$

Starting with the gas dynamic equations, it is shown that across two paths in the $x - t$ plane two compatibility conditions are satisfied.

$$u + \frac{2}{\gamma - 1}c = r \qquad u - \frac{2}{\gamma - 1}c = s$$

The constants r and s are known as *Riemann invariants* and will be used heavily in later analysis.

THIS PAGE INTENTIONALLY LEFT BLANK

Chapter 3

Analysis of the evolution of the head rarefaction wave in a shock tube

The basic functioning of a shock tube is well understood and has been extensively studied, (e.g. [11]). A shock tube consists of a driver section containing gas—commonly helium or air—at high pressure, and a driven section, initially separated by a membrane, Fig. 3-1(a). Upon rupture of the membrane, a shock wave propagates towards the driven section followed by a contact discontinuity, whereas a family of rarefaction waves propagates in the opposite direction within the driver section, Fig. 3-1(b). While unperturbed by the end sections of the shock tube, the flow responds to the well known Riemann solution, [20]. Here, we are interested in the various wave interactions taking place upon the reflection of the head rarefaction wave at the left end of the driver section. In the subsequent evolution of the flow, the reflected head wave reaching the right-propagating shock marks the onset of the Friedlander wave form in the shock tube. Figure 3-1 shows snapshots of the shock tube at different times emphasizing the location of key flow characteristics (shock, contact discontinuity, head and tail waves) as well as the evolution of the spatial pressure distribution. To help the analysis we make heavy use of Figure 3-2 which shows the evolution of the characteristic lines in the x-t plane.

The basic idea of the analysis is to track the evolution (velocity history) of the head and trailing rarefaction waves in the various stages of their interaction with the flow: 1) propagation towards the left closed end of the tube, Fig. 3-1(b), 2) interaction with trailing rarefaction waves after reflection at the closed end, Fig. 3-1(c), 3) propagation towards the moving contact discontinuity, Fig. 3-1(d) 4) interaction with the contact discontinuity, Fig. 3-1(e), and 5) propagation towards the shock, Fig. 3-1(f).

Next, we focus on determining the location in the shock tube where this occurs. The determination of the location of the onset of the Friedlander wave form only requires tracking the evolution of the head wave. Immediately after the membrane ruptures, Fig. 3-1(b), the constant speed of the head wave using (2.11) is $a_4 = \sqrt{\gamma_4 p_4/\rho_4}$ where a_4, γ_4, p_4 and ρ_4 are, respectively, the sound speed, the specific heat ratio, the pressure and the density in the undisturbed region of the driver section. It is worth emphasizing that the parameters on the right-hand side of this equation constitute basic input settings of the shock tube. The time t_a at which the head rarefaction wave reaches the closed end of the shock tube, Fig. 3-1(c) and point a in Fig. 3-2, is simply given by:

$$t_a = \frac{L_1}{a_4} \tag{3.1}$$

After time t_a, the flow in the shock tube departs from the classical Riemann problem and the head rarefaction wave enters a non-simple region: the first buffer region.

3.1 Analysis of the first buffer region

The first buffer region comprises the zone where the centered fan of rarefaction waves interacts with the closed end of the tube, Figures 3-1(c), 3-2, and 3-3(a). Riemann [12] originally proposed a mathematical formulation of this problem in the form of an Euler-Poisson partial differential equation (PDE) governing the time $t(r, s)$ at which two characteristics with coordinates (r, s) meet inside the buffer region. He obtained a general solution for a gas with arbitrary specific heat ratio γ. However, the solution is difficult to use in the analysis of the further evolution of the flow in the shock tube, as it is given in implicit form in terms of a hypergeometric function. Landau and

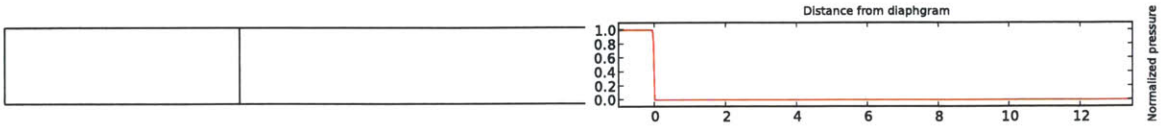

(a) Initial Configuration of the Shock tube.

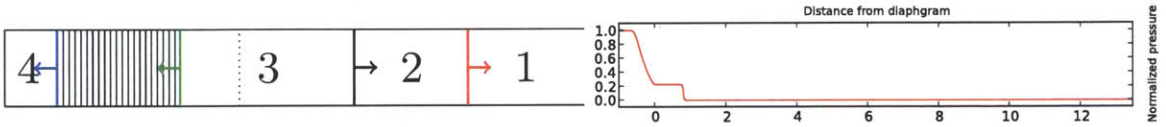

(b) Riemann structure of the flow following diaphragm rupture.

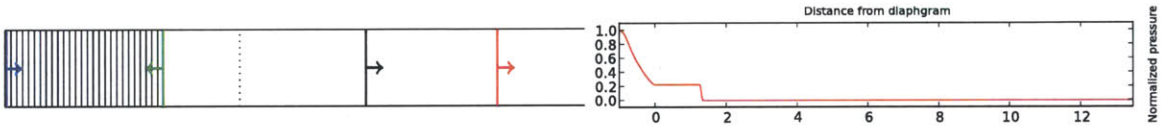

(c) The head wave arrives at the wall.

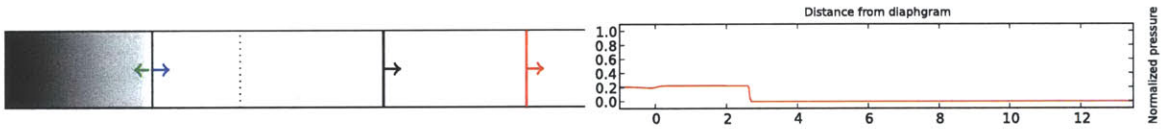

(d) The head wave exits the buffer region after reaching the tail wave.

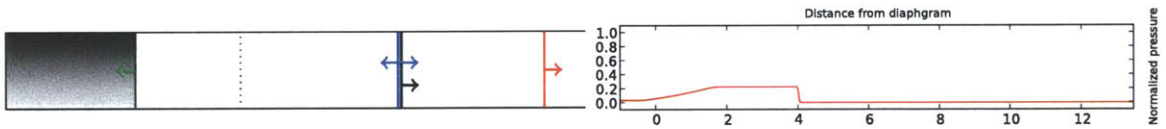

(e) The head wave arrives at the contact interface.

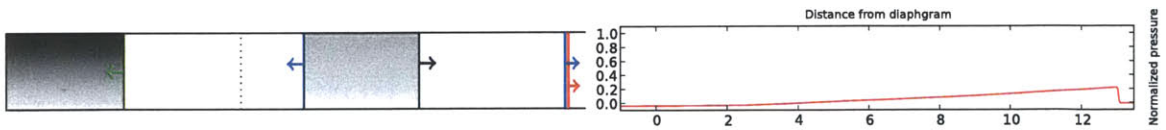

(f) The head wave arrives at the shock wave.

Figure 3-1: Schematic of the evolution of the shock wave structure in the shock tube (left figures) and evolution of the pressure profile (right figures).

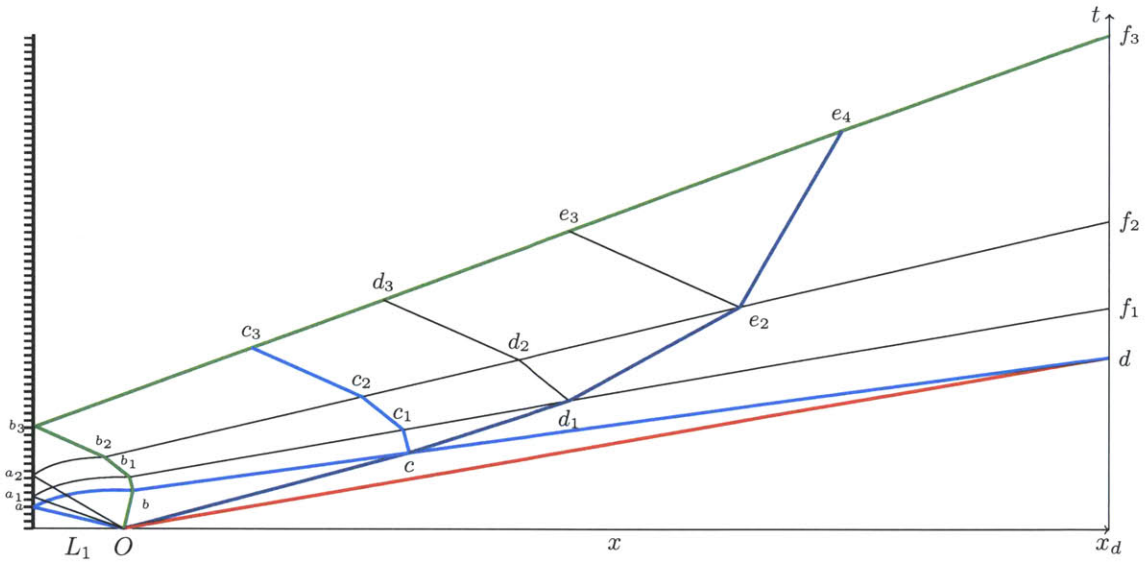

Figure 3-2: The interaction of waves in a shock tube in the $x - t$ space of characteristics. The shock wave is represented by the red characteristic whereas the light blue and the green ones are the head and the tail rarefaction waves respectively. The contact interface is the dark blue characteristic curve.

Lifschitz [17] derived an explicit expression of the exit time of the head rarefaction wave from the buffer region for monoatomic ($\gamma = \frac{5}{3}$) and diatomic ($\gamma = 1.4$) gases, based on a reformulation of the PDE using the Legendre transformation. Here, we propose a third alternative derivation which is limited to the cases of practical interest (air and helium), but has the great advantage of providing a full solution for $t(r, s)$ in explicit form in terms of a simple rational function.

3.1.1 Arriving at the Euler-Darboux PDE

Fig. 3-3(a) shows a plot in the (x, t) plane of the characteristics of the head wave, the tail wave and two sample intermediate rarefaction waves as they propagate toward the closed end of the driver section, reflect off the wall and interact with each other in the first buffer region. Prior to entering the first buffer region, rarefaction waves move at constant speed along a straight characteristic. Any arbitrary point A inside the buffer region lies at the intersection of two rarefaction waves, a right-going wave along a C_+ characteristic and a left-going wave along a C_- characteristic. The wave

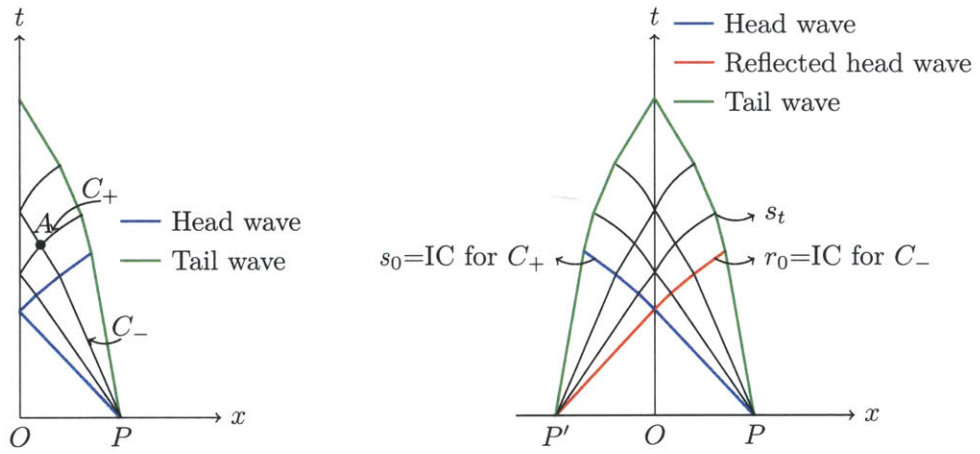

Figure 3-3: (a) The reflection of rarefaction waves from a wall and interaction in the first buffer region (b) Using the method of images to address the initial conditions at the wall, highlighting the boundaries of the first buffer region.

speed for these two waves is given respectively by:

$$\begin{aligned} U^+ &= \tfrac{dx}{dt}\big|_{C_+} = u + a \\ U^- &= \tfrac{dx}{dt}\big|_{C_-} = u - a \end{aligned} \tag{3.2}$$

where $u = u(x,t)$ is the local gas speed and $a = a(x,t)$ is the local sound speed. On any given characteristic, C_+ or C_-, the evolution of these quantities is governed by the Riemann invariants [14] as follows:

$$\begin{aligned} r &:= u + \tfrac{2a}{\gamma-1} = const. \ \text{ along } C_+ \\ s &:= u - \tfrac{2a}{\gamma-1} = const. \ \text{ along } C_- \end{aligned} \tag{3.3}$$

Furthermore, the local gas speed u and the local sound speed a can be conveniently expressed in terms of the Riemann invariants r and s as follows:

$$u = \frac{1}{2}(r+s) \quad \text{and} \quad a = \frac{\gamma-1}{4}(r-s) \tag{3.4}$$

On a C_+ characteristic, the position x at a time t of a right-going wave only depends on the value of the Riemann invariant s of intersecting C_- characteristics. Conversely,

on a C_- characteristic, the position x at a time t of a left-going wave depends only on the Riemann invariants r of the intersecting C_+ characteristics. These features of the Riemann invariants motivate the change of variables from space-time (x,t)-coordinates to characteristic space (r,s)-coordinates.

We aim to determine the time $t(r,s)$ at which an incoming left-going rarefaction wave meets a right-going rarefaction wave reflected from the rigid wall. From (3.2) and using the invariance of r and s along C_+ and C_- respectively, we obtain:

$$\frac{\partial x}{\partial s} = (u+a)\frac{\partial t}{\partial s} \tag{3.5}$$

$$\frac{\partial x}{\partial r} = (u-a)\frac{\partial t}{\partial r} \tag{3.6}$$

The x variable can be eliminated by invoking the equality of mixed partials to arrive at:

$$2a\frac{\partial^2 t}{\partial r \partial s} + \frac{\partial (u+a)}{\partial r}\frac{\partial t}{\partial s} - \frac{\partial (u-a)}{\partial s}\frac{\partial t}{\partial r} = 0 \tag{3.7}$$

Rewriting the gas (u) and sound (a) speeds in terms of the Riemann invariants using (3.4), this expression can be further simplified into a PDE for the time variable t only:

$$\frac{\partial^2 t}{\partial r \partial s} - \frac{\lambda}{r-s}\left(\frac{\partial t}{\partial r} - \frac{\partial t}{\partial s}\right) = 0 \quad \text{where} \quad \lambda = \frac{1}{2}\left(\frac{\gamma+1}{\gamma-1}\right) \tag{3.8}$$

This is a second-order hyperbolic partial differential equation of the Euler-Darboux type. In the particular cases of air and helium, λ is an integer: $\lambda = 3$ for air ($\gamma_4 = 1.4$) and $\lambda = 2$ for helium ($\gamma_4 = \frac{5}{3}$). A general solution of the Euler-Darboux PDE for integer valued λ can be written in terms of arbitrary functions of a single variable: f and g, in the following form [21]:

$$t(r,s) = \frac{\partial^{2\lambda-2}}{\partial r^{\lambda-1}\partial s^{\lambda-1}}\left(\frac{f(r)-g(s)}{r-s}\right) \tag{3.9}$$

3.1.2 Describing initial conditions

The functions f and g in (3.9) are determined from the initial conditions of the problem, which correspond to the time at which any rarefaction wave enters the first

buffer region. Left-going rarefaction waves, emitted from the center P and traveling on C_- characteristics, enter the buffer region when they intersect the reflected right-going head wave (in red in Fig. 3-3(a)). On this characteristic of Riemann invariant r_0, the derivative of the position x and the time t with respect to the invariant s are related through (3.5). Using (3.4), this expression reads:

$$\frac{dx}{ds} = \left(\frac{1+\gamma}{4}r_0 + \frac{3-\gamma}{4}s\right)\frac{dt}{ds} \tag{3.10}$$

Further, any point along the characteristic of the right-going head wave is also the end point of the straight characteristic of some left-going rarefaction wave of the form: $x = (u-a)t + x_P$, where x_P is the location of the center of the rarefaction fan. Differentiating this expression with respect to s and combining with (3.4) yields another relation between the derivatives of the position x and time t with respect to the invariant s:

$$\frac{dx}{ds} = \left(\frac{3-\gamma}{4}r_0 + \frac{1+\gamma}{4}s\right)\frac{dt}{ds} + \left(\frac{1+\gamma}{4}\right)t \tag{3.11}$$

The variable x is eliminated by taking the difference between (3.10) and (3.11) and simplifying, resulting in the following ODE:

$$\frac{dt}{ds} - \frac{\lambda}{r_0 - s}t = 0 \tag{3.12}$$

Right-going reflected rarefaction waves traveling on C_+ characteristics enter the first buffer region at the time they reflect off the wall. However, due to the hyperbolic nature of the problem, these times depend on the solution of the PDE inside the buffer region itself. This issue is easily circumvented by recourse to the method of images, see e.g. [22], by which the problem can be replaced with the interaction of two centered fans as shown in Fig. 3-3(b). In this case, the C_- characteristic s_0 can be determined by an ODE analogous to (3.12):

$$\frac{dt}{dr} - \frac{\lambda}{r - s_0}t = 0 \tag{3.13}$$

Solving both ODEs, we arrive at an explicit expression of the entry time of the left-going rarefaction waves, $t(r_0, s)$, and the right-going rarefaction waves, $t(r, s_0)$, on the red and blue curves that bounds the buffer region in Fig. 3-3(b) respectively:

$$t(r_0, s) = t_a \left(\frac{r_0 - s_0}{r_0 - s} \right)^{\lambda} \tag{3.14}$$

$$t(r, s_0) = t_a \left(\frac{r_0 - s_0}{r - s_0} \right)^{\lambda} \tag{3.15}$$

3.1.3 Solving the flow problem in the buffer region

The initial conditions, (3.14), (3.15) can now be used to determine the functions $f(r)$ and $g(s)$ in (3.9). In the case of air ($\lambda = 3$), the solution (3.9) can be written as:

$$t(r, s) = 2\frac{f''(r) - g''(s)}{(r - s)^3} - 12\frac{f'(r) + g'(s)}{(r - s)^4} + 24\frac{f(r) - g(s)}{(r - s)^5} \tag{3.16}$$

where primes denote derivatives of f and g with respect to their single argument. Evaluating (3.16) at the two initial conditions $t(r, s_0)$, (3.14), and $t(r_0, s)$, (3.15), yields two independent ODEs for f and g, respectively:

$$\begin{aligned}(r - s_0)^2 f''(r) - 6(r - s_0)f'(r) + 12f(r) = (g''(s_0) + \frac{t_a}{2}(r_0 - s_0)^3)(r - s_0)^2 \\ + 6g'(s_0)(r - s_0) + 12g(s_0)\end{aligned} \tag{3.17}$$

$$\begin{aligned}(r_0 - s)^2 g''(s) + 6(r_0 - s)g'(s) + 12g(s) = (f''(r_0) - \frac{t_a}{2}(r_0 - s_0)^3)(r_0 - s)^2 \\ - 6f'(r_0)(r_0 - s) + 12f(r_0)\end{aligned} \tag{3.18}$$

Here, we are interested in any solutions $f(r)$ and $g(s)$ that satisfy the condition $t(r_0, s_0) = t_a$, i.e. the first buffer region starts at the time that the head rarefaction wave arrives at the fixed wall, (3.1). We may choose any initial conditions for the ODEs (3.17) and (3.18) as long this condition is satisfied. We choose $f(r_0) = 1$, $f'(r_0) = 1$, $f''(r_0) = \frac{t_a}{2}(r_0 - s_0)^3$, $g(s_0) = 1$, $g'(s_0) = -1$ and $g''(s_0) = 0$. This yields

an explicit form for the two ODEs:

$$(r-s_0)^2 f''(r) - 6(r-s_0)f'(r) + 12f(r) = \frac{t_a}{2}(r_0-s_0)^3(r-s_0)^2 - 6(r-s_0) + 12 \tag{3.19}$$

$$(r_0-s)^2 g''(s) + 6(r_0-s)g'(s) + 12g(s) = -6(r_0-s) + 12 \tag{3.20}$$

Assuming the solutions to (3.19), (3.20) are respectively of the form $(r-s_0)^m$, $(r_0-s)^m$, the solutions of the corresponding homogeneous problems are given by $\{(r-s_0)^3, (r-s_0)^4\}, \{(r_0-s)^3, (r_0-s)^4\}$. The particular solutions can be obtained by inspection as: $a_1(r-s_0)^2 + a_2(r-s_0) + a_3$, and $b_1(r_0-s) + b_2$, respectively. The general solution can then be obtained by the method of undetermined coefficients inserting these expressions in the ODEs and solving for the coefficients, leading to:

$$f(r) = 2\frac{(r-s_0)^3}{(r_0-s_0)^2} - \frac{(r-s_0)^4}{(r_0-s_0)^3} - (r-s_0) + 1 + \frac{t_a}{4}(r_0-s_0)(r-s_0)^2(r-r_0)^2 \tag{3.21}$$

$$g(s) = 2\frac{(r_0-s)^3}{(r_0-s_0)^2} - \frac{(r_0-s)^4}{(r_0-s_0)^3} - (r_0-s) + 1 \tag{3.22}$$

Using a similar approach, the solution of (3.9) for the case of helium ($\lambda = 2$) can be obtained in the form:

$$t(r,s) = \frac{f'+g'}{(r-s)^2} - 2\frac{f-g}{(r-s)^3} \quad \text{where} \quad \begin{cases} f(r) = t_a(r_0-s_0)(r-s_0)(r-r_0) + 1 \\ g(s) = 1 \end{cases} \tag{3.23}$$

3.1.4 Computing the head wave exit time from the buffer region: t_b

The head rarefaction wave of Riemann invariant r_0 exits the buffer region when it meets the tail rarefaction wave of Riemann invariant s_t at time $t_b = t(r_0, s_t)$, Fig. 3-3(b). Conversely, t_b can be viewed as the time the tail rarefaction wave enters the first buffer region. Its value is then easily computed from the initial condition of

the Euler-Darboux PDE for the left-going rarefaction waves (3.14) in terms of the Riemann invariants s_t, r_0 and s_0. In the Riemann solution, the head wave moves to the left into the undisturbed region of the driver section, denoted region 4 in Fig. 3-1(a). In this region the local gas velocity is 0 and the local sound speed is a_4. The tail wave moves left from the region behind the contact interface, denoted region 3 in Fig. 3-1(a). In this region the local gas velocity is u_p and the local sound speed is a_3. The Riemann invariants r_0, s_0 and s_t are obtained using (3.3):

$$r_0 = \frac{2a_4}{\gamma_4 - 1} \qquad s_0 = -\frac{2a_4}{\gamma_4 - 1} \qquad s_t = u_p - \frac{2a_3}{\gamma_4 - 1} \tag{3.24}$$

We replace (3.24) in (3.16), further relate a_3 to a_4 using the isentropic relation: $a_3 = a_4 - \frac{\gamma_4 - 1}{2} u_p$ and obtain:

$$t(r_0, s_t) = t_a \left(\frac{1}{1 - \frac{\gamma_4 - 1}{2} \left(\frac{u_p}{a_4} \right)} \right)^{\lambda} \tag{3.25}$$

The denominator can be simplified by using the isentropic equation that relates the constant pressure behind the contact interface (p_3) to the initial pressure in the driver section(p_4):

$$\frac{p_3}{p_4} = \left(1 - \frac{\gamma_4 - 1}{2} \left(\frac{u_p}{a_4} \right) \right)^{\frac{2\gamma_4}{\gamma_4 - 1}}$$

With the above equation and noting that the pressure is preserved across the contact interface, $p_3 = p_2$, (3.25) reduces to:

$$t_b = t_a \left(\frac{p_4}{p_2} \right)^{\frac{\lambda(\gamma_4 - 1)}{2\gamma_4}} \quad \text{with} \quad \begin{cases} \lambda = 3 \text{ for air} \\ \lambda = 2 \text{ for helium} \end{cases} \tag{3.26}$$

From the time of exit equations for air and helium, we can see that the head wave exits sooner in helium than air. Note that the expression for t_b can be read from the initial condition (3.14) with no need for one to solve the PDE explicitly. However it is important to see that this solution provides time of intersection of two waves given r and s. We will take advantage of this solution in the next chapter where we

compute analytical estimates of the parameters of the pressure profile at the onset of the Friedlander wave.

3.2 Subsequent wave interactions and determination of the Friedlander wave onset location

The location at which the head rarefaction wave exits the first buffer region can be computed from the time t_b it took the tail rarefaction wave to travel at constant speed $u_p - a_3$ and enter the first buffer region. At this location: $t_b(u_p - a_3)$, the head wave enters a simple wave region and travel at constant speed $u_p + a_3$ until it meets the contact interface moving at constant speed u_p. We denote as t_c the time the two waves meet which is obtained from equating the time it took for the contact interface to reach the meeting location $u_p t_c$ from its location at t_b: $u_p t_b$ with the time it took for the head rarefaction wave to reach it on the right-hand side:

$$\frac{u_p t_c - u_p t_b}{u_p} = \frac{u_p t_c - (u_p - a_3)t_b}{a_3 + u_p} \tag{3.27}$$

We note that the resulting expression for $t_c = 2t_b$ holds independently of the type of driver gas (air or helium).

The transmitted head wave through the contact interface enters a simple wave region and travels at constant speed $u_p + a_2$ until it meets the shock wave. At t_c the shock wave is located at Wt_c and the head wave is located at $(u_p + a_2)t_c$. The time for the head wave to reach the shock front, t_d, can be found from the following equality:

$$\frac{Wt_d - Wt_c}{W} = \frac{Wt_d - u_p t_c}{u_p + a_2} \quad \text{as} \quad t_d = \frac{2t_b a_2}{u_p + a_2 - W} \tag{3.28}$$

where W, u_p and a_2 are, respectively, the shock speed, the speed of the contact discontinuity and the sound speed behind the shock which are all determined from

the Riemann problem as:

$$W = a_1\sqrt{\frac{\gamma_1+1}{2\gamma_1}\left(\frac{p_2}{p_1}-1\right)+1}$$

$$u_p = \frac{a_1}{\gamma_1}\left(\frac{p_2}{p_1}-1\right)\sqrt{\frac{\frac{2\gamma_1}{\gamma_1+1}}{\frac{p_2}{p_1}+\frac{\gamma_1-1}{\gamma_1+1}}}$$

$$a_2 = a_1\sqrt{\frac{p_2}{p_1}\frac{\frac{\gamma_1+1}{\gamma_1-1}+\frac{p_2}{p_1}}{1+\frac{\gamma_1+1}{\gamma_1-1}\left(\frac{p_2}{p_1}\right)}}$$

Here $a_1 = \sqrt{\gamma_1 p_1/\rho_1}$ where a_1, γ_1 , p_1 and ρ_1 are, respectively, the sound speed, the specific heat ratio, the pressure and the density in the undisturbed region of the driven section. The unknown pressure behind the shock wave, p_2, can be determined by solving the implicit relation below [14]:

$$\frac{p_4}{p_1} = \frac{p_2}{p_1}\left\{1-\frac{(\gamma_4-1)(\frac{a_1}{a_4})(\frac{p_2}{p_1}-1)}{\sqrt{2\gamma_1\left(2\gamma_1+(\gamma_1+1)(\frac{p_2}{p_1}-1)\right)}}\right\}^{\frac{-2\gamma_4}{\gamma_4-1}} \tag{3.29}$$

The determination of t_d completes our analysis since, given the length of the driver section L_1, the location at which the Friedlander wave forms is given by:

$$L = L_1 + Wt_d \tag{3.30}$$

In the next chapter, we will provide analytical estimates of parameters that govern the pressure decay at this location.

3.2.1 Computation procedure for minimum shock tube length

Given the initial inputs in the shock tube, 1 provides an algorithm to compute the onset location of a Friedlander wave.

Algorithm 1 Computation of minimum shock tube length and Friedlander wave peak pressure

1: **Input parameters:** L_1, γ_1, p_1, T_1, γ_4, p_4, T_4

2: **Compute:** $a_1 = \sqrt{\gamma_1 R T_1}$ and $a_4 = \sqrt{\gamma_4 R T_4}$

3: **Compute:** peak pressure p_2 implicitly defined as: $\frac{p_4}{p_1} = \frac{p_2}{p_1}\left\{1 - \frac{(\gamma_4-1)(\frac{a_1}{a_4})(\frac{p_2}{p_1}-1)}{\sqrt{2\gamma_1\left(2\gamma_1+(\gamma_1+1)(\frac{p_2}{p_1}-1)\right)}}\right\}^{\frac{-2\gamma_4}{\gamma_4-1}}$

4: **Compute:** $u_p = \frac{a_1}{\gamma_1}\left(\frac{p_2}{p_1}-1\right)\sqrt{\frac{\frac{2\gamma_1}{\gamma_1+1}}{\frac{p_2}{p_1}+\frac{\gamma_1-1}{\gamma_1+1}}}$ and $a_2 = a_1\sqrt{\frac{p_2}{p_1}\frac{\frac{\gamma_1+1}{\gamma_1-1}+\frac{p_2}{p_1}}{1+\frac{\gamma_1+1}{\gamma_1-1}\frac{p_2}{p_1}}}$

5: **Compute:** $W = a_1\sqrt{\frac{\gamma_1+1}{2\gamma_1}\left(\frac{p_2}{p_1}-1\right)+1}$

6: **Compute:** $t_d = \frac{2L_1 a_2}{a_4(u_p+a_2-W)}\left(\frac{p_4}{p_2}\right)^{\frac{(\gamma_4+1)}{4\gamma_4}}$

7: **Result:** Friedlander onset location $L = L_1 + W t_d$

THIS PAGE INTENTIONALLY LEFT BLANK

Chapter 4

Analysis of the pressure profile of a Friedlander wave at onset location

The arrival of rarefaction waves trailing the head wave contribute to the pressure decay and, with their successive arrival times, describe the pressure history at the Friedlander onset location. The determination of pressure behind the shock wave in terms of the initial parameters in the driven section (speed of sound: a_1, pressure: p_1 and density: ρ_1) is in general difficult because of the nonuniform entropy evolution behind the shock. The change in the left-going Riemann invariant s across the shock discontinuity evolves with the third power of the shock strength defined as $z = \frac{p-p_1}{p_1}$. For weak to medium shocks ($z \leq 5$), the Riemann invariant s may be considered constant through the shock [23]. Practically, this amounts to neglecting any rarefaction waves reflecting off the shock front. Further, the pressure across a shock wave agrees up to second order in the shock strength with the pressure across a simple wave given by:

$$\frac{p}{p_1} = \left(1 - \frac{\gamma_1 - 1}{2}\left(\frac{u}{a_1}\right)\right)^{\frac{2\gamma_1}{\gamma_1 - 1}} \tag{4.1}$$

Equivalently, the pressure at the onset location can be expanded in terms of the local gas velocity u—continuously modified by the incoming rarefaction waves—up

to second order [15], leading to:

$$p = p_1 + \rho_1 a_1 u + \frac{\gamma_1 + 1}{4}\rho_1 u^2 \tag{4.2}$$

The computation of the local gas velocity u at L involves tracking the path of the incoming rarefaction waves. From the time it exits the first buffer region to the time it arrives at the Friedlander onset location, any rarefaction wave travels through the contact discontinuity. Because the gas on both sides of this interface are in different thermodynamical states, part of the incoming rarefaction wave is transmitted through, and part of it is reflected off, the contact interface. The reflected part then interacts with the trailing incoming rarefaction waves in a second simple wave interaction region: the second buffer region. Unlike the first buffer region, this region consists of non-centered rarefaction waves interacting with a moving boundary, which precludes a simple mathematical treatment. Therefore, we consider only a finite number of rarefaction waves in the fan and adopt in the sequel a discrete approach.

The local gas speed along any right going rarefaction wave of invariant r evolves with the successive values of the Riemann invariants s of intersecting left-going simple waves. The discrete approach then seeks to determine the left-going Riemann invariant at the intersection of a right-going rarefaction waves with any left-going waves, eventually leading to the value of the gas velocity using (3.4), and thus the value of the pressure using (4.2), at the onset location. Further, the estimation of the arrival time of any rarefaction wave involves computing the time and position of all the considered wave intersections from the moment it exits the first buffer region.

4.1 Determination of the exit time and position of a rarefaction wave from first buffer region

As shown in Fig. 3-3(a), rarefaction waves, reflected off the closed end of the shock tube, exit the first buffer region when they intersect the tail wave. The explicit analytical solution (3.16) determines the exact time at which this happens. The

exit speed for any given rarefaction wave is given by $U_+ = u + a$ where u and a are determined from the Riemann invariants r and s_t using (3.4). To compute the position at which each rarefaction wave exits the first buffer region, we assume that any rarefaction wave travels on a straight path and at the average velocity between any two successive wave intersections. For instance in Fig. 3-2, paths: $b \to b1$, $b1 \to b2$ and $b2 \to b3$ are linear. The position x_{b_i} at which the i-th rarefaction wave exits, at time t_{b_i} with the wave speed U_{b_i}, the first buffer region can be estimated from the exit position $x_{b_{i-1}}$, exit time $t_{b_{i-1}}$ and exit speed $U_{b_{i-1}}$ of the immediately preceding rarefaction wave as:

$$x_{b_i} = x_{b_{i-1}} + \frac{1}{2}(U_{b_{i-1}} + U_{b_i})(t_{b_i} - t_{b_{i-1}}) \tag{4.3}$$

We recall that the exit time and position of the head rarefaction wave are respectively given by t_b (3.26) and $x_{b_0} = (u_p - a_3)t_b$, thus completing the recurrence relation (4.3).

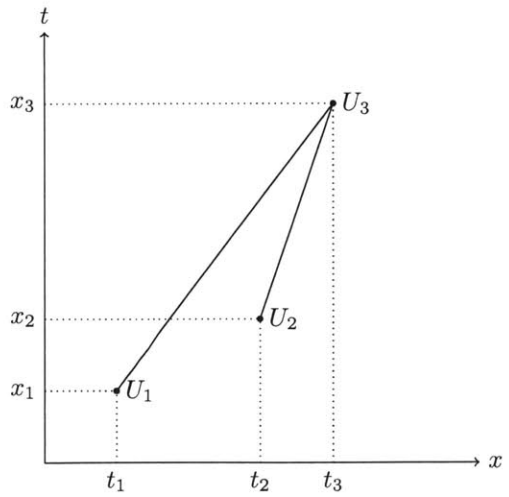

Figure 4-1: A schematic of two waves intersecting in the (x, t) plane

4.2 Determination of the time and position of a rarefaction wave at each intersection point in the second buffer region

Inside the second buffer region, the computation of time and position for each intersection point can be done as follows. Consider the intersection of two waves in the (x,t) plane as depicted in Fig. 4-1. At time t_1, the first wave is located at x_1 traveling at a faster speed, U_1, than the speed U_2 of the second wave which, at time t_2, is located at x_2. At a later time t_3, they intersect at some position x_3 where their common wave speed is U_3. It is assumed that each wave travels at average of the velocity between the two intersection points: $\frac{1}{2}(U_1+U_3)$ for the first wave and $\frac{1}{2}(U_2+U_3)$ for the second. The meeting position x_3 and time t_3 of the two waves are simply given by:

$$x_3 = \frac{x_1(U_2+U_3) - x_2(U_1+U_3)}{U_2-U_1} \qquad t_3 = t_1 + 2\frac{x_3-x_1}{U_1+U_3}$$

The determination of the position and time for each wave interaction inside the second buffer region requires then knowing the wave velocity at each intersection.

4.3 Determination of the velocity of a rarefaction wave at each intersection point in the second buffer region

Inside the second buffer region, the local gas (u) and sound speed (a) can be determined at any wave intersection from the left- and right-going Riemann invariants using (3.4). The Riemann invariant r of any rarefaction wave is known from the Riemann problem. The Riemann invariants s along left-going characteristics are not constant across the contact discontinuity. Ahead of this interface, all these characteristics originate from a simple region. Thus, their common Riemann invariant s is

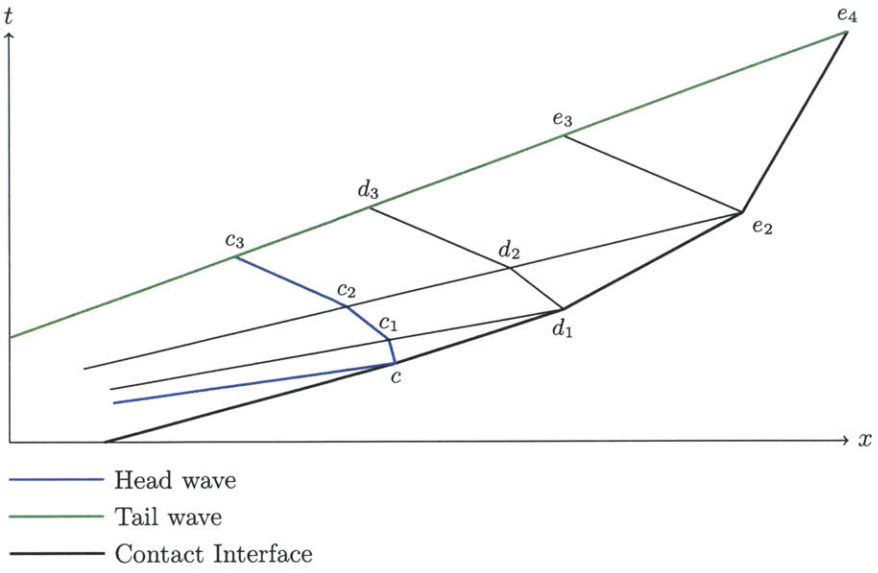

Figure 4-2: Rarefaction waves exiting the first buffer region interact with the contact interface

equal to $u_p - \frac{2}{\gamma_1 - 1} a_2$ where u_p is the velocity of the contact discontinuity and a_2 is the sound speed behind the shock front in the Riemann problem. Behind the contact discontinuity, each left-going characteristic has a unique Riemann invariant that can be determined from the unknown gas velocity and sound speed.

Consider the point d_1 in Fig. 4-2 on the contact interface. We can write the right-going invariant in terms of the local gas velocity $u^L_{d_1}$ and $a^L_{d_1}$ immediately on the left of d_1 and the left-going invariant interms of the local gas velocity $u^R_{d_1}$ and $a^R_{d_1}$ immediately on the right of d_1 using (3.3). We recall that the local gas velocity is preserved across the contact discontinuity: $u_{d_1} = u^L_{d_1} = u^R_{d_1}$.

$$u_{d_1} + \frac{2}{\gamma_1 - 1} a^L_{d_1} = r \tag{4.4}$$

$$u_{d_1} - \frac{2}{\gamma_1 - 1} a^R_{d_1} = u_p - \frac{2}{\gamma_1 - 1} a_2 \tag{4.5}$$

We relate the the sound speeds on both sides of d_1 with respect to the sound speed on both sides of point c where the head rarefaction wave meets the contact discontinuity. To the right of the contact interface, we relate the sound speeds at d_1 and c. With the speed of sound given by $a = \sqrt{\gamma RT}$, using the isentropic relation that relates the

pressure and temperature and recalling that the pressure is also preserved across the contact discontinuity ($p^R_{d_1} = p^L_{d_1} = p_{d_1}$ and $p^R_{c_1} = p^L_{c_1} = p_{c_1}$), we obtain:

$$\frac{a^R_{d_1}}{a^R_c} = \sqrt{\frac{T^R_{d_1}}{T^R_c}} = \sqrt{\left(\frac{p_{d_1}}{p_{c_1}}\right)^{\frac{\gamma_1 - 1}{\gamma_1}}} \tag{4.6}$$

To the left of the contact interface, we relate the sound speeds at d_1 and c and proceed in a similar manner as above leading to the following equation:

$$\frac{p_{d_1}}{p_c} = \left(\frac{a^L_{d_1}}{a^L_c}\right)^{\frac{2\gamma_4}{\gamma_4 - 1}} \Rightarrow a^R_{d_1} = a^R_c \left(\frac{a^L_{d_1}}{a^L_c}\right)^{\frac{\gamma_4(\gamma_1 - 1)}{\gamma_1(\gamma_4 - 1)}} \tag{4.7}$$

From the Riemann problem, a^L_c and a^R_c are the sound speed behind the contact interface(a_3) and the sound speed behind the shock front(a_2) respectively. Using (4.7) in (4.5) and simplifying, the following equation that relates the local gas speed to the local sound speed to the left of the contact interface [15] is obtained:

$$u_{d_1} - u_p = \left[\left(\frac{a^L_{d_1}}{a_3}\right)^{\frac{\gamma_4(\gamma_1 - 1)}{\gamma_1(\gamma_4 - 1)}} - 1\right] \frac{2a_2}{\gamma_1 - 1} \tag{4.8}$$

If the gas in both sections of the shock tube is air , $\gamma_1 = \gamma 4 = 1.4$, (4.8) gives us an explicit constraint on the relationship of the local gas speed and sound speed at all the points on the contact interface. With two unknowns $u_{d_1}, a^L_{d_1}$ and two equations (4.8) and (4.4), the local gas speed and sound speed at d_1 are completely determined. Since the point d_1 is an arbitrary point on the contact interface, the conclusion that the local gas speed and sound speed are completely determined is applicable for all the points on the boundary of the contact interface . The Riemann invariant s along the reflected rarefaction waves can be computed using (3.3). With r and s fully determined, the local gas speed and sound speed at all interior points in the second buffer region can be computed from (3.4).

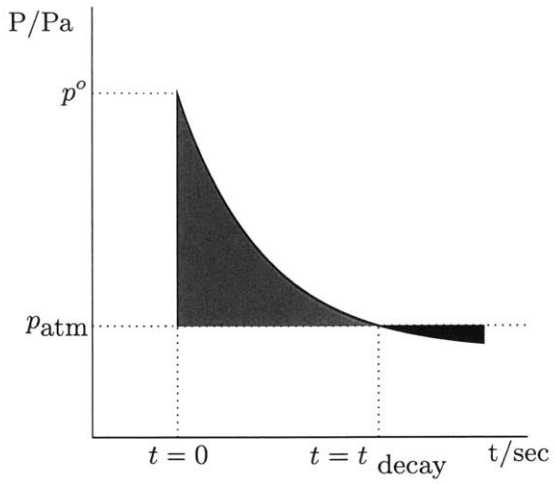

Figure 4-3: The pressure profile of a Friedlander wave

4.4 Determination of the pressure profile

The pressure history of a Friedlander wave, as depicted in Fig. 4-3, at a fixed location in space is fully characterized by its peak overpressure, decay time and impulse [24, 25]. The peak overpressure, p^0, is the difference between the maximum pressure and the atmospheric pressure. The time interval during which the blast pressure is greater than the atmospheric pressure is the decay time(t_{decay}). The impulse, I, is the positive area under the pressure time curve. The Friedlander form is given by a quasi-exponential equation:

$$p = p^0 \left(1 - \frac{t}{t_{\text{decay}}}\right) e^{\frac{-\alpha t}{t_{\text{decay}}}} \tag{4.9}$$

The impulse is calculated by integrating (4.9) up to the decay time

$$I = p^0 t_{\text{decay}} \left(\frac{1}{\alpha} - \frac{1}{\alpha^2}(1 - e^{-\alpha})\right) \tag{4.10}$$

The wave form parameter, α, is then the root of the equation below that can be obtained numerically by Newton's method.

$$p^0 t_{\text{decay}} \left(\alpha + e^{-\alpha} - 1\right) - \alpha^2 I = 0 \tag{4.11}$$

To characterize the pressure history at L, the arrival of four rarefaction waves is considered. These are the head wave, the tail wave and two intermediate rarefaction waves as shown in Fig. 3-2. The head wave arrives at time t_d and the initial pressure is equal to the pressure behind the shock in the Riemann problem(p_2). Let (t_{f_1}, p_{f_1}),(t_{f_2}, p_{f_2}) and (t_{f_3}, p_{f_3}) be the arrival time and pressure at L for the two intermediate rarefaction waves and the tail wave respectively. The peak overpressure is trivially determined equating to p_2. The remaining parameters, decay time and impulse, can be computed as follows. At the arrival of the second rarefaction wave, the pressure at L is above atmospheric pressure while at the arrival of the tail wave, the pressure at L is below atmospheric pressure. The straight line defined by the two points (t_{f_2}, p_{f_2}), (t_{f_3}, p_{f_3}) is given by:

$$p = (1 - t_{f_3}) \left(\frac{p_{f_3} - p_{f_2}}{t_{f_3} - t_{f_2}} \right) t + p_{f_3} \tag{4.12}$$

The time at which the pressure is atmospheric, t_{atm}, is the x intercept of (4.12).

$$t_{\text{atm}} = \frac{(p_{\text{atm}} - p_{f_3})}{(1 - t_{f_3}) \left(\frac{p_{f_3} - p_{f_2}}{t_{f_3} - t_{f_2}} \right)} \tag{4.13}$$

With this, the decay time is simply:

$$t_{\text{decay}} = t_{\text{atm}} - t_d \tag{4.14}$$

The impulse is determined through numerical integration by Trapezoidal rule using the four data points.

Chapter 5

Verifications against numerical simulations

5.1 Numerical approach

In order to assess the predictability of the analytical approach proposed in this paper, we compare the different analytical estimates against results obtained numerically using the CFD code AMROC (Adaptive Mesh Refinement in Object-oriented C++) which is part of the Virtual Test Facility (VTF) [26]. The fluid domain comprised in a shock-tube of constant section is described as 2D rectangle of length being set on a case-by-case basis so as to make sure that the shock and then blast wave is still present in the computational domain at the end of the simulation. Hence, the effect of the opening of the shock-tube of the flow has been purposefully not taken into account. The height of the rectangular computational domain has been set to 1 meter which is typically a very large diameter for a laboratory scale shock-tube. Still, it allowed us to verify the assumption that the flow in a shock-tube is essentially one-dimensional since we did not observe any significant difference in the flow along the direction of the height of the tube. The simulation should run long enough to be able to see the pressure decaying from the maximum pressure to the atmospheric pressure and then decreasing to the negative phase.

To guide the simulations from the above considerations, we use our analytical

model. The total time of the simulation should be greater than the sum of t_d and t_{decay} which can be obtained from equations (3.28) and (4.14) respectively. The initial conditions in the tube are as follows: we prescribed the initial value of the pressure in the driver section in a rectangular region of same length on the left-hand side of the computational domain. The reminder of the tube is set to atmospheric pressure. In both regions, the temperature is set to be ambient and equal to 300K; the gas density is computed from the equation of state of perfect gas. It is also worth noting that only the air-driven shock tube has been modeled with AMROC, the biphase flow corresponding helium driven shock tube has not been simulated.

The numerical framework provides frequent snapshots of the spatial distribution of the thermodynamical quantities describing the flow: the pressure, the energy density, the flow velocity and its density. This feature could in principle be used to pinpoint the location in the tube at which the head rarefaction wave catches up with the shock wave when the pressure plateau is reduced to a point and the pressure starts decaying. However, this transition from a shock wave to a blast wave is very slow, thus, making it hard to choose the location of the blast onset with certainty. Alternatively, AMROC can also provide the time evolution of these quantities at a prescribed location within the flow. We use this latter feature to examine how the pressure time profile obtained numerically closely matched the predicted analytical estimates. In particular, we compare the overpressure, the decay time, the impulse and the wave form parameter obtained numerically and analytically. For both approaches, the impulse has been computed by numerical integration from the data point, the value of α following from (4.11).

5.2 Results

5.2.1 Friedlander wave Location

Tab. 5.1 presents, for compressed air driven shock tube, the evolution of the predicted blast onset location as the initial pressure in the driver pressure is increased so as to

produce a blast of incident overpressure approximatively equal to 1.5, 2.0, 3.0 and 4.0 times the atmospheric pressure respectively. For each of these four cases, the length of the driver section is also varied from 0.25 m to 1.0 m. We see that the length at which we predict a blast wave first forms increases with the increase of the driver length. However, the blast onset location reaches a minimum value for a driver pressure close to 440.0 kPa consistently for all the 4 driver lengths considered. Fig. 5-1 illustrates the time evolution of the pressure at the analytical blast onset location for all the 16 cases of different driver lengths and initial pressures for both the analytical model and the numerical approach.

At all the analytically predicted blast onset locations, we observe the numerical pressure profile of fully formed blast waves, thus demonstrating the validity of the analytical model. We remark that the value of the maximum incident pressure predicted by the solution of the Riemann problem agrees very well with the numerical results with a maximum error of less than 2%. Further, as expected, the maximum incident pressure is not affected by the driver length. The three analytical predicted values: (p_{f_1}, t_{f_1}), (p_{f_2}, t_{f_2}) and (p_{f_3}, t_{f_3}) (see Fig. 3-2) describing the pressure decay with time past the initial peak value fall in all 16 cases almost on the top of the curve obtained numerically. We notice that, for low ratio peak incident overpressures 1.5 and 2.0, the pressure evolution with respect to time is accurately described by the four points computed analytically. For the other two cases, corresponding to a stronger shock regime, these four points are not fully capturing the pressure decay with time subsequent to the initial peak overpressure. In the next subsection, we offer a more quantitative examination for how a description of the pressure evolution with these four points match the numerical results.

5.2.2 Friedlander wave Pressure Profile

Tab. 5.2 presents the comparison between the analytical and numerical pressure profiles of the blast wave by considering the decay time, impulse and the wave form parameter at the analytical location of blast formation for air driven shock tube. We consider different shock tube configurations by varying the driver pressure and driver

Driver Pressure	Incident Pressure		Length	Blast Location L	
	air	helium		air	helium
(kPa)	(kPa)	(kPa)	(m)	(m)	(m)
234.0	152	186	0.25	4.89	1.33
			0.50	9.79	2.67
			0.75	14.68	4.00
			1.00	19.57	5.34
440.0	202.7	276.5	0.25	4.14	1.19
			0.50	8.28	2.38
			0.75	12.43	3.57
			1.00	16.57	4.76
1153.1	304.0	503.1	0.25	4.47	1.32
			0.50	8.95	2.64
			0.75	13.42	3.96
			1.00	17.90	5.28
2452.8	405.3	770.1	0.25	5.33	1.58
			0.50	10.66	3.17
			0.75	15.99	4.75
			1.00	21.32	6.33

Table 5.1: Comparison of blast wave onset locations and incident pressures between compressed air and compressed helium shock tube.

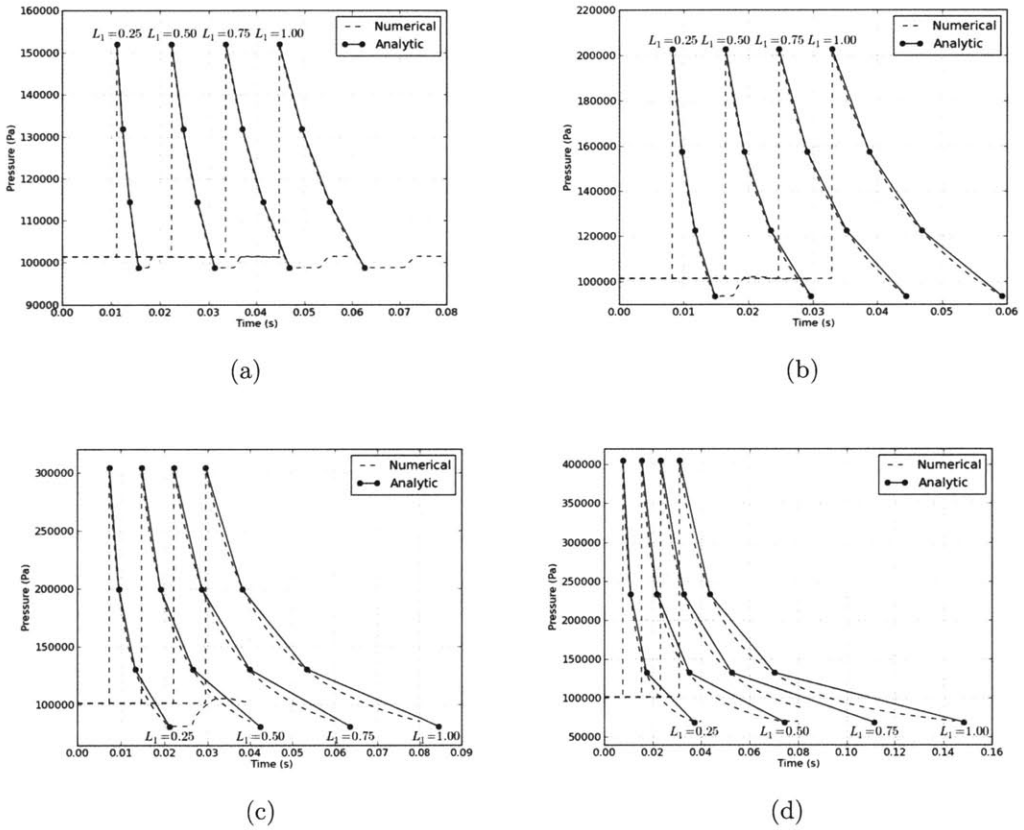

Figure 5-1: Numerical *vs* Analytical Pressure Profiles for: (a) $\frac{p_2}{p_1} \approx 1.5$, (b) $\frac{p_2}{p_1} \approx 2.0$, (c) $\frac{p_2}{p_1} \approx 3.0$ and (d) $\frac{p_2}{p_1} \approx 4.0$

length. As before, the pressure in the driver pressure is increased so as to produce a blast of incident overpressure approximatively equal to 1.5, 2.0, 3.0 and 4.0 times the atmospheric pressure. For each of these four cases, the length of the driver section is also varied from 0.25 m to 1.0 m.

For a fixed driver pressure, we notice that the decay time and impulse increase almost linearly with increasing driver lengths. Inversely, for a fixed driver length, the decay time and impulse increase with increasing driver pressure. As such, we see that the decay time and impulse are minimized for shock tubes with short driver section and low driver pressure. In the analytical model, unlike the decay time and impulse, the wave form parameter is independent of the of the driver length or driver pressure. However there is a slight variation of the parameter in the numerical simulations with a maximum standard deviation of about 0.05. The error between the numerical and analytical approach for the pressure profile parameters increases with increasing driver pressure. The error increases from $\approx 2\%$ to $\approx 20\%$ and from $\approx 5\%$ to $\approx 15\%$ for the decay time and impulse respectively as one goes from the lowest driver pressure to the highest driver pressure.

5.2.3 Influence of the driver gas on the peak pressure and Friedlander wave location

The type of driver gas in the driver section affects the peak pressure, the location of the onset of the blast and the pressure profile parameters: decay time, impulse and the wave form parameter. From (3.29) and (3.30), the peak pressure and the blast onset location can be computed. Tab. 5.1 presents a comparison of these parameters between air and helium used as a driver gas for different shock tube configurations. As before, the pressure in the driver section is increased so as to produce a blast of incident overpressure approximatively equal to 1.5, 2.0, 3.0 and 4.0 times the atmospheric pressure. For each of these four cases, the length of the driver section is also varied from 0.25 m to 1.0 m. From Tab. 5.1 we observe that helium driven shock tube has higher peak pressures than air driven shock tubes and the ratio of

Driver Section		Driven Section								
Pressure	Length	Decay time			Impulse			Wave Form Parameter		
(kPa)	(m)	ana. (ms)	num. (ms)	err. (%)	ana. (Pa.s)	num. (Pa.s)	err. (%)	ana.	num.	err. (%)
234.0	0.25	4.1	4.1	2.3	89.2	84.2	5.7	0.5	0.5	2.0
	0.50	8.3	8.1	1.8	178.5	170.5	4.5	0.5	0.5	1.9
	0.75	12.4	12.2	2.1	267.7	256.9	4.1	0.5	0.5	0.0
	1.00	16.9	16.3	3.2	357.0	346.4	2.9	0.5	0.5	0.0
440.0	0.25	5.8	5.5	5.1	216.9	201.6	7.1	1.0	0.9	5.5
	0.50	11.5	11.0	4.5	433.8	409.0	5.7	1.0	0.9	3.2
	0.75	17.3	16.5	4.5	650.7	613.4	5.7	1.0	0.9	2.1
	1.00	23.0	22.0	4.3	867.5	823.7	5.1	1.0	1.0	1.1
1153.1	0.25	10.6	9.2	12.5	631.4	562.8	10.9	1.8	1.6	12.2
	0.50	21.1	18.6	12.1	1262.8	1140.6	9.7	1.8	1.7	10.2
	0.75	31.7	27.8	12.1	1894.2	1710.9	9.7	1.8	1.7	9.5
	1.00	42.2	37.1	12.1	2525.6	2281.2	9.7	1.8	1.7	9.5
2452.8	0.25	19.4	15.0	22.4	1379.7	1174.8	14.8	2.9	2.3	22.7
	0.50	38.8	30.0	22.6	2759.3	2348.6	14.9	2.9	2.4	21.2
	0.75	58.1	45.0	22.6	4139.0	3509.1	15.2	2.9	2.4	20.7
	1.00	77.5	60.0	22.6	5518.7	4700.1	14.8	2.9	2.4	20.2

Table 5.2: Characterizing the decay time, impulse and wave form parameter for different driver length and driver section pressure

the peak pressures(helium/air) increases as one increases the driver pressure. For the lowest driver pressure, the peak overpressure is almost the same. However in the case of the highest driver pressure, the peak pressure for the helium driven shock tube is almost twice the corresponding value for air driven shock tube. For both air and helium driven shock tubes, the location of the blast onset is directly proportional to the driver length. We also notice that the formation of blast wave occurs closer to the diaphragm in the case of helium driven shock tubes. For all the cases considered, the blast location for helium is about 3 times shorter than air.

5.2.4 Comparison with existing shock-tubes

Tab. 5.3 compares the peak overpressure and blast location of the Wayne State University helium driven shock tube (WSU) described in [27], and later used in [3], to the analytical model. The WSU shock-tube measures 7.12 m and possesses three pressure sensors: the "R-wall" sensor, the "Trigger" sensor, the "Pencil" sensor located at 2.80 m, 5.57 m and 5.98 m from the closed end of the tube. The time evolution of the pressure at these different locations are reported in [3]. At the "R-wall" location, the pressure profile exhibits the short plateau indicating that head rarefaction wave has not yet caught up with the shock wave whereas the pressure profile at the 2 other locations are those of fully formed blast waves. We estimate the experimental incident pressure by looking at the value of the plateau pressure at the "R-wall" senor. We estimate the recording during the acquisition of the pressure to be of the order of 7 kPa. At the different sensor locations, the maximum recorded pressure have not noticeably decayed over a span of almost 3 m. For this experimental setup, our analytical model predicts that the blast wave should form 4.02 m away from the closed end of the tube which is at distance almost two meters shorter than the experimental location.

Shock Tube	Driver		Overpressure		Blast Location	
	Length (m)	Pressure (kPa)	Experimental (kPa)	Analytic (kPa)	Experimental (m)	Analytic (m)
WSU [27]	0.76	241	83±7	84	5.97	4.02

Table 5.3: Comparison of overpressure and blast location between experimental and analytical method

5.2.5 On the fitness of the Friedlander functional form and the analytical model

Tab. 5.4 presents a comparison of the impulses obtained from the numerical simulations using two different methods using direct numerical integration by the trapezoidal rule and using the expression of the impulse from the Friedlander mathematical form (4.10) with the values of the decay time (t_d) and of the wave form parameter (α) provided by a non-linear least-square fit on the numerical data points. We use the error between the fitted impulse and the numerical impulse as a metric for how well the numerical profile resembles the Friedlander form. As shown in Tab. 5.4, the error is always below 2%, thus demonstrating that the blast wave produced by a shock-tube is very accurately described by the Friedlander form.

Driver	Initial Pressure (kPa)	234.0				440.0			
	Length (m)	0.25	0.50	0.75	1.00	0.25	0.50	0.75	1.0
Driven	Impulse								
	Numerical (Pa.s)	84.2	170.5	256.9	346.4	201.6	409.0	613.4	823.7
	Fitted (Pa.s)	84.0	170.4	256.5	345.8	201.0	408.0	612.0	822.0
	Error (%)	0.1	0.1	0.1	0.2	0.3	0.3	0.2	0.2
Driver	Initial Pressure (kPa)	1153.1				2452.8			
	Length (m)	0.25	0.50	0.75	1.00	0.25	0.50	0.75	1.00
Driven	Impulse								
	Numerical (Pa.s)	562.8	1140.6	1711.0	2281.2	1174.8	2348.6	3509.1	4700.1
	Fitted (Pa.s)	558.3	1131.4	1697.5	2263.4	1153.8	2306.0	3446.5	4614.8
	Error (%)	0.8	0.8	0.8	0.8	1.8	1.8	1.8	1.8

Table 5.4: Comparison of Numerical Impulse to the Impulse of fitted Friedlander form

5.3 Discussion

Compressed-gas driven shock tubes have been used experimentally as small scale alternatives to open field blast tests[9, 10, 8]. In free field, the pressure profile of blast waves at a fixed location is best described by the Friedlander form [24, 25]. This quasi-exponential equation has three important parameters: peak pressure, decay time and impulse. The placement of a specimen inside a shock tube is an important consideration. A non-optimal location inside the shock tube will expose the specimen to a Trapezoidal wave form which is unlike a blast wave[1]. To date, only numerical or empirical techniques have been employed to characterize the formation of a blast wave inside a shock tube. In this study, we provided an analytical model to determine the location at which a blast wave forms inside a compressed gas driven shock tube and computed the pressure profile parameters at that location. We also identify three design parameters: driver length, driver initial pressure and driver gas, that a practitioner can act upon to design a shock tube producing a blast wave of desired peak overpressure, decay time and impulse.

By analyzing the wave interaction inside a shock tube, an explicit equation (3.30) for the location at which a blast wave forms inside compressed air driven shock tube was derived. Using an asymptotic analysis, we provide an estimate for the peak overpressure, decay time and impulse at the location. For compressed helium driven shock tube, an analogous analysis allows us to compute the location of the blast onset and the peak overpressure. The study also presents the first analytical verification that a blast wave forms much earlier in a compressed helium shock tube than in a compressed air shock tube. The strength of our model resides in the fact that it is purely analytical, very easy to use and facilitates easy implementation as opposed to the only available alternative offered by the CFD approach. To the best of our knowledge, Kleinschmit et.al[13, 7] were the first to investigate whether a Friedlander wave forms in a shock tube. We show the first quantified confirmation that a Friedlander wave actually forms inside a shock tube.

The asymptotic analysis for the estimate of the pressure profile parameters for

compressed air shock tubes is limited by number of intermediate rarefaction waves. The results from our current model which is based on four rarefaction waves shows that, as shown in fig. 5-1(a)-(b), the analysis captures the pressure profile very well for weak to medium shock waves$\left(\frac{p_2}{p_1} < 3\right)$ but there is a loss of accuracy as the shock regime becomes stronger $\left(\text{fig. 5-1(c)-(d)}\right)$. For strong shock waves, we posit that the number of rarefaction waves needed for accurate representation of the profile does not greatly exceed four, and as such, the current model is quite adequate even for these edge cases.

Practitioners have considered the placement of specimen at or near the opening of a shock tube [13, 27]. At this location, the temporal evolution of the pressure after its initial peak is modified by the outside flow and this mandates an analysis which is not considered in our current analytical model. Kleinschmit *et al.* recommend to put the test specimen deep inside the tube [13, 7] since the pressure profile at this open end doesn't resemble a blast wave. As such, this aspect is not a serious limitation of the current model.

THIS PAGE INTENTIONALLY LEFT BLANK

Chapter 6

Conclusion

In this study, we have developed an analytical model for an informed design of a shock tube. By a thorough analysis of the different wave interactions, we have derived an explicit expression for the location at which a Friedlander wave forms inside compressed air driven shock tube. Using an asymptotic analysis, we provide an estimate for the decay time, impulse and wave form parameter at this location. An analogous analysis leads us to to compute the onset of blast and peak overpressure for compressed helium shock tube. We show that blast wave forms faster if one uses helium instead of air in the driver section. Our analysis agrees very well with numerical simulations. Using these simulations, we have demonstrated that the blast wave formed inside a shock tube follows the Friedlander form.

6.1 Recommendations for Future Work

The author proposes extension of the work presented in this thesis in the following directions:

- A useful extension to this work would be to create a suitable design chart or an inverse estimate mobile/web application that will aid in the design of shock tubes. Given a specimen at some location inside a shock tube, a practitioner is interested in computing the driver pressure and driver length to be able to produce a blast wave of of desired peak overpressure, decay time and impulse. Our

analytical model is simple enough to use so that inverse methods or optimization techniques can implement it.

- Some of the theoretical work in this thesis has the possibility for extension. The first one is the extension of the asymptotic analysis for compressed helium driven shock tube. In this case, with helium as the driver gas and air as the driven gas($\gamma_1 \neq \gamma_4$), (4.8) requires further analysis.

- A third future work is to extend the model to non-constant shock tubes. Our current analytical model is one-dimensional and only holds for constant-section shock tubes. However, some shock tubes with non-constant cross sections have been designed [13, 27]. In such cases, the analysis of flow after the rupture of the diaphragm requires a modification. Chisnell [28] has solved the problem of the propagation of shock waves through regions of non-uniform tube. One could take advantage of this analysis and integrate it into our analytical formulation .

Appendix A

Solution of the Euler Darboux PDE for helium driven shock tube

For helium driven shock tube, $\lambda = 2$, the solution (3.9) can be simplified in terms of first derivative noted $(.)'$ of f and g with respect to r and s:

$$t(r,s) = -2\frac{f' + g'}{(r-s)^2} - 2\frac{f-g}{(r-s)^3} \tag{A.1}$$

Evaluating (A.1) at the two initial conditions $t(r, s_0)$, (3.14), and $t(r_0, s)$, (3.15), yields two independent ODEs for f and g, respectively:

$$(r-s_0)f' - 2f = -2g_0 + t_a(r_0-s_0)^2(r-s_0) - g_0'(r-s_0) \tag{A.2}$$

$$(r_0-s)g' - 2g = -2f_0 + t_a(r_0-s_0)^2(r_0-s) - f_0'(r_0-s) \tag{A.3}$$

where f_0 and f_0' refer to the function f and its first derivative evaluated at r_0 and g_0 and g_0' refer to the function g and its first derivative evaluated at s_0. We determine these constants from the expression of the time at which the head rarefaction wave arrives at the fixed wall in terms of r_0 and s_0, $t_a = t(r_0, s_0)$. We arbitrarily choose $f_0 = 1$, $g_0 = 1$ and $g_0' = 0$ which in turn determine $f_0' = t_a(r_0 - s_0)^2$. (A.2) and (A.3)

simplify to:

$$(r - s_0)f' - 2f = -2 + t_a(r_0 - s_0)^2(r - s_0) \tag{A.4}$$

$$(r_0 - s_)g' - 2g = -2 + t_a(r_0 - s_0)^2(r_0 - s) - t_a(r_0 - s_0)^2(r_0 - s) \tag{A.5}$$

These second order non-homogeneous ODEs admit a unique solution. One can verify that the following expressions are their respective solution:

$$f(r) = t_a(r_0 - s_0)(r - s_0)(r - r_0) + 1 \tag{A.6}$$

$$g(s) = 1 \tag{A.7}$$

Appendix B

A Python class to compute the onset of the Friedlander wave in a shock tube

This section provides a Python code to compute the peak pressure p_2 and the minimum lnegth of a shock tube L needed for Friedlander wave formation. The full details of the computation can be found in 3. As part of this thesis, I have written codes to compute the decay time, impulse and wave form parameter at the Friedlander onset location. They are quite lengthy to be included here but all the codes are available at `http://aftasiss.scripts.mit.edu/abiy/codes`.

```
# SI Units for all parameters, CI stands for contact interface
"""
The class computes the peak pressure and minimum length of a shock tube
for Friedlander wave formation given the initial input parameters.
"""
import math,pylab
import numpy as np
from numpy import array
from scipy.optimize import brentq
import matplotlib.pyplot as plt
from matplotlib.pylab import *

class ShockTube:
    #Instantiate class
    def __init__(self,gamma1,gamma4,p1,p4,T1,T4,L1):
```

```
  #Initial pressure
    self.p1=p1
    self.p4=p4
  #Initial temperature
    self.T1=T1
    self.T4=T4
  #Gamma
    self.gamma1=gamma1
    self.gamma4=gamma4
  # Length of the driver section
    self.L1=L1
  #pressure ratios
    self.p4p1=self.p4/self.p1
  # Calculate initial densities
    self.rho1=self.p1/(287.0*self.T1)
    self.a1=math.sqrt((self.gamma1*self.p1)/self.rho1)
    if self.gamma4==1.4:
        self.rho4=self.p4/(287.0*self.T4)
        self.a4=math.sqrt((self.gamma4*self.p4)/self.rho4)
    if self.gamma4==1.66:
        self.rho4=self.p4/(2080.0*self.T4)
        self.a4=math.sqrt((self.gamma4*self.p4)/self.rho4)
  #Speed of sound in the two regions
    self.p2p1=self.newton_solver(self.p4p1)
  # For simplification purposes:
    self.CONSTANT1=((self.gamma1+1.0)/(self.gamma1-1.0))

# Function: Finds P2 from the implicit Relation
def pressure_function(self,x,y):
    self.p4p1num=(self.gamma4-1)*(self.a1/self.a4)*(x-1)
    self.p4p1dnm=math.sqrt(2*self.gamma1*(2*self.gamma1+(self.gamma1+1)*(x-1)))
    return y-x*(1-(self.p4p1num/self.p4p1dnm))**((-2.0*self.gamma4)/(self.gamma4-1.0));

# Function: Netwon solver for pressure, using brentq from scipy
def newton_solver(self,y):
    self.p2p1= brentq(self.pressure_function,1,self.p4p1,args=(y))
    return self.p2p1

# Function: Solves all parameters behind the shock wave
def return_p2(self):
    self.p2=self.p2p1*self.p1
    return self.p2
def return_T2(self):
    t2t1=self.p2p1*((self.CONSTANT1+self.p2p1)/(1.0+self.CONSTANT1*self.p2p1))
    self.T2=t2t1*self.T1
    return self.T2
def return_rho2(self):
    rho2rho1=(1+self.CONSTANT1*self.p2p1)/(self.CONSTANT1+self.p2p1)
    self.rho2=rho2rho1*self.rho1
    return self.rho2
```

```
# Return the shock speed W
def return_W(self):
    self.W=self.a1*math.sqrt(((self.gamma4+1)/(2*self.gamma4))*(self.p2p1-1)+1)
    return self.W
# Return the speed of the gas behind the shock wave i.e up
def return_up(self):
    rho2=self.return_rho2()
    self.up=self.W*(1-(self.rho1/rho2))
    return self.up
# Return the sound speed behind the shock a2
def return_a2(self):
    self.a2=math.sqrt((self.gamma1*self.p2)/self.rho2)
    return self.a2
# Compute parameters behind the contact interface
def return_p3(self):
    p3p4=self.p2p1/self.p4p1
    self.p3=p3p4*self.p4
    return self.p3
def return_T3(self):
    p3p4=self.p2p1/self.p4p1
    T3T4=(p3p4)**((self.gamma4-1)/self.gamma4)
    self.T3=T3T4*self.T4
    return self.T3
def return_rho3(self):
    p3p4=self.p2p1/self.p4p1
    rho3rho4=(p3p4)**(1/self.gamma4)
    self.rho3=rho3rho4*self.rho4
    return self.rho3

# return the speed of sound behind the contact interface
def return_a3(self):
    self.a3a4=1-(((self.gamma4-1)/(2.0))*(self.up/self.a4))
    self.a3=self.a3a4*self.a4
    return self.a3
# Return the speed of the head wave
def return_uh(self):
    #uh is the speed of the head wave
    self.uh=-1*self.a4
    return self.uh
# Return the speed of the tail wave
def return_ut(self):
    #ut is the speed of the tail wave
    self.ut=self.up-self.a3
    return self.ut
#Function: Solves all parameters of interest for the LHS(between tail and head)
def return_p5(self,x,t):
    u=(2.0/(self.gamma4+1.0))*(self.a4+x/t)
    CONSTANT2=(0.5*(self.gamma4-1))*(u/self.a4)
    CONSTANT3=1-CONSTANT2
    p5p4=(CONSTANT3)**((2.0*self.gamma4)/(self.gamma4-1.0))
```

```
    p5=p5p4*self.p4
    return p5
def return_T5(self,x,t):
    u=(2.0/(self.gamma4+1.0))*(self.a4+x/t)
    CONSTANT2=(0.5*(self.gamma4-1))*(u/self.a4)
    CONSTANT3=1-CONSTANT2
    T5T4=(CONSTANT3)**2.0
    T5=T5T4*self.T4
    return T5
def return_rho5(self,x,t):
    u=(2.0/(self.gamma4+1.0))*(self.a4+x/t)
    CONSTANT2=(0.5*(self.gamma4-1))*(u/self.a4)
    CONSTANT3=1-CONSTANT2
    rho5rho4=(CONSTANT3)**((2)/(self.gamma4-1.0))
    rho5=rho5rho4*self.rho4
    return rho5

#Function: Compute the time it takes for the rarefaction wave to catch up with the
#shock wave front. time_one is the time it takes the head wave to reach the end wall
def time_1(self):
    self.time_one=self.L1/self.a4
    return self.time_one
#time_two is the time in the buffer region
def time_2(self):
    if self.gamma4==1.4:
        self.time_two=self.time_one*((self.p4/self.p2)**
                    ((3*self.gamma4-3)/(2*self.gamma4)))
    if self.gamma4==1.66:
        self.time_two=self.time_one*((self.p4/self.p2)**
                    ((self.gamma4-1)/(self.gamma4)))
    U12=self.a4+0.5*self.up
    self.time_two_approx=self.time_one+(self.L1-self.time_one*(self.a3-self.up))/(U12)
    return self.time_two
#time_three is the time to meeting the CI
def time_3(self):
    self.time_three=2*(self.time_two)
    return self.time_three
#time_four is the time to catch the shock front
def time_4(self):
    self.time_four=(2*self.time_two*self.a2)/(self.up+self.a2-self.W)
    return self.time_four
#The total time elapsed is simply the sum of each time duration
def time_total(self):
    self.time_total=self.time_four
# The minimum total length of the tube
# for Friedlander wave formation
def minimum_length(self):
    self.len_min=self.a4*self.time_one+self.W*(self.time_total)
    return self.len_min
```

The input file *input_shocktube.txt* and the driver *main_shock_tube.py* are provided below.

```
# gamma1: driven section
1.4
# gamma4: driver section
1.4
# pressure of the driven section: p1
101325.0
# pressure of the driver section: p4
1013250.0
# T1: Temperature of gas at driven section(usually air)
300.0
# T4: Temperature of gas at driver section(usually air or Helium)
300.0
#Length of the driver section in m
0.25
```

```
import os
from ShockTube import ShockTube
def main():
        input_file = open("input_shock_tube.txt",'r')
        lines = input_file.readlines()
        gamma1 = float(lines[1])
        gamma4 = float(lines[3])
        p1 = float(lines[5])
        p4 = float(lines[7])
        T1 = float(lines[9])
        T4 = float(lines[11])
        pos=float(lines[13])
        shock_tube=ShockTube(gamma1,gamma4,p1,p4,T1,T4,pos)
        shock_tube.return_p2()
        shock_tube.return_W()
        shock_tube.return_up()
        shock_tube.return_a3()
        shock_tube.return_uh()
        shock_tube.return_ut()
        shock_tube.return_p3()
        shock_tube.return_T2()
        shock_tube.return_T3()
        shock_tube.return_rho2()
        shock_tube.return_rho3()
        shock_tube.return_a2()
        shock_tube.return_a3()
        shock_tube.time_1()
        shock_tube.time_2()
        shock_tube.time_3()
        shock_tube.time_4()
        shock_tube.time_total()
        shock_tube.minimum_length()
        shock_tube.print_values("output_shock_tube.txt")
```

THIS PAGE INTENTIONALLY LEFT BLANK

Bibliography

[1] Nakagawa A., Manley G.T., Gean A.D., Ohtani K., Armonda R., Tsukamoto A., Yamamoto H., Takayama K., and Tominaga T. Mechanisms of primary blast-induced traumatic brain injury: Insights from shock-wave research. *Journal of Neurotrauma*, 28:1335–1342, 2011. pdf.

[2] Ibolja Cernak, Andrew C. Merkle, Vassilis E. Koliatsos, Justin M. Bilik, Quang T. Luong, Theresa M. Mahota, Leyan Xu, Nicole Slack, David Windle, and Farid A. Ahmed. The pathobiology of blast injuries and blast-induced neurotrauma as identified using a new experimental model of injury in mice. *Neurobiology of Disease*, 41(2):538 – 551, 2011. pdf, DOI.

[3] Alessandra Dal Cengio Leonardi, Cynthia A. Bir, Dave V. Ritzel, and Pamela J. VandeVord. Intracranial pressure increases during exposure to a shock wave. *Journal of Neurotrauma*, 28(1):85–94, Jan 2011. pdf, DOI.

[4] Matthew B Panzer, Kyle A Matthews, Allen W Yu, Barclay Morrison, David F Meaney, and Cameron R Bass. A multiscale approach to blast neurotrauma modeling: Part I - Development of novel test devices for in vivo and in vitro blast injury models. *Frontiers in Neurology*, 3(46), 2012. pdf, DOI.

[5] Sundaramurthy A., Alai A., Ganpule S., Holmberg A., Plougonven E., and Chandra N. Blast-induced biomechanical loading of the rat: An experimental and anatomically accurate computational blast injury model. *Journal of Neurotrauma*, 29:2352–2364, 2012. pdf.

[6] Amy C. Courtney, Lubov P. Andrusiv, and Michael W. Courtney. Oxy-acetylene driven laboratory scale shock tubes for studying blast wave effects. *Review of Scientific Instruments*, 83(4):045111, 2012. pdf, DOI.

[7] N. Chandra, S. Ganpule, N.N. Kleinschmit, R. Feng, A.D. Holmberg, A. Sundaramurthy, V. Selvan, and A. Alai. Evolution of blast wave profiles in simulated air blasts: experiment and computational modeling. *Shock Waves*, 22(5):403–415, 2012. pdf, DOI.

[8] Cameron Bass, Matthew B. Panzer, Karen A. Rafaels, Garrett Wood, Jay Shridharani and Bruce Capehart. Brain Injuries from Blast. *Annals of Biomedical Engineering*, 40:185–202, 2012. pdf, DOI.

[9] Raj K Gupta and Andrzej Przekwas. Mathematical models of blast induced TBI: current status, challenges and prospects. *Frontiers in Neurology*, 4(59), 2013. pdf, DOI.

[10] Ye Xiong, Asim Mahmood, and Michael Chopp. Animal models of traumatic brain injury. *Nat Rev Neurosci*, 14(2):128–142, 2013. pdf, DOI.

[11] H. W. Liepmann and A. Roshko. *Elements of Gasdynamics.* Dover, 2002.

[12] B. Riemann. Uber die Fortpflanzung ebener Luftwellen von endlicher Schwingungswei. *Abhandlungen der Gesellsehaft der Wissenschaften zu Gottingen, Math.-physikal.*, 8:43–65, 1860.

[13] Nicholas Kleinschmit. A Shock Tube Technique for Blast Wave Simulation and Studies of Flow Structure Interactions in Shock Tube Blast Experiments. Master's thesis, University of Nebraska-Lincoln, 2011. pdf.

[14] J. D. Anderson. *Modern Compressible Flow: With Historical Perspective.* McGraw-Hill, New York, 2003.

[15] R. Courant and K.O. Friedrichs. *Supersonic Flow and Shock Waves.* Interscience Publishers, New York, 1999.

[16] Enrico Fermi. *thermodynamics.* Dover Publications, New York, 1956.

[17] L.D. Landau and E.M. Lifscitz. *Fluid Mechanics.* Pergamon Press, 1987.

[18] Ya.B.Zeldovich and Yu.P.Raizer. *Physics of Shock Waves and High-Temperature Hydrodynamic Phenomena.* Academic Press, New York and London, 1966.

[19] Sandro Salsa. *Partial Differential Equations: From Modelling to Theory.* Springer, New York , 1966.

[20] Bernhard Riemann. *Collected papers.* Heber City, UT : Kendrick Press, c2004., 2004.

[21] N. S. Koshlyakov, M. M. Smirnov, and E. B. Gliner. *Differential Equations of Mathematical Physics.* North-Holland Publishing Company, Amsterdam, 1964.

[22] A. H. Taub. Interaction of Progressive Rarefaction Waves. *Annals of Mathematics*, 47(4):811–828, 1946. pdf.

[23] G. B. Whitham. *Linear and Nonlinear waves.* John Wiley and Sons, 1974.

[24] F. G. Friedlander. The Diffraction of Sound Pulses. I. Diffraction by a Semi-Infinite Plane. *Proceedings of the Royal Society of London. Series A, Mathematical and Physical Sciences*, 186(1006):322–344, 1946. pdf, DOI.

[25] J. M. Dewey. The Air Velocity in Blast Waves from t.n.t. Explosions. *Proceedings of the Royal Society of London. Series A. Mathematical and Physical Sciences*, 279(1378):366–385, 1964. pdf, DOI.

[26] R. Deiterding, R. Radovitzky, S.P. Mauch, L. Noels, J.C. Cummings, and D. Meiron. A virtual test facility for the efficient simulation of solid material response under strong shock and detonation wave loading. *Engineering with Computers*, 22:325–347, 2006.

[27] Alessandra Dal Cengio Leonardi. *An investigation of the biomechanical response from shock wave loading to the head.* PhD thesis, Wayne State University, 2011. pdf.

[28] R. F. Chisnell. The motion of a shock wave in a channel, with applications to cylindrical and spherical shock waves. *Journal of Fluid Mechanics*, 2:286–298, 1957. .